Remote Sensing of Environment 319 (2025) 114636

Contents lists available at ScienceDirect

Remote Sensing of Environment

journal homepage: www.elsevier.com/locate/rse

DART-based temporal and spatial retrievals of solar-induced chlorophyll fluorescence quantum efficiency from *in-situ* and airborne crop observations

Omar Regaieg [a,*], Zbyněk Malenovský [a], Bastian Siegmann [b], Jim Buffat [b], Julie Krämer [b], Nicolas Lauret [c], Valérie Le Dantec [c]

[a] *University of Bonn, Department of Geography, Germany*
[b] *Forschungszentrum Jülich GmbH, IBG-2: Plant Sciences, Germany*
[c] *Centre d'Etudes Spatiales de la Biosphère UT3-CNES-CNRS-IRD-INRAE, France*

ARTICLE INFO

Edited by Jing M. Chen

Keywords:
Photosystem-level solar-induced fluorescence
Physical downscaling
Radiative transfer modeling
3D canopy structure
Photosynthesis
Canopy biochemical properties

ABSTRACT

Remotely sensed top-of-the-canopy (TOC) SIF is highly impacted by non-physiological structural and environmental factors that are confounding the photosystems' emitted SIF signal. Our proposed method for scaling TOC SIF down to photosystems' (PSI and PSII) level uses a three-dimensional (3D) modeling approach, capable of accounting physically for the main confounding factors, *i.e.*, SIF scattering and reabsorption within a leaf, by canopy structures, and by the soil beneath. Here, we propose a novel SIF downscaling method that separates the structural component from the functional physiological component of TOC SIF signal by using the 3D Discrete Anisotropic Radiative Transfer (DART) model coupled with the leaf-level fluorescence model Fluspect-CX, and estimates the Fluorescence Quantum Efficiency (FQE) at photosystem level. The method was first applied on *in-situ* diurnal measurements acquired at the top of the canopy of an alfalfa crop with a near-distance point-measuring FloX system. The retrieved photosystem-level FQE diurnal courses correlated significantly with photosynthetic yield of PSII measured by an active leaf florescence instrument MiniPAM ($R = 0.87$, $R^2 = 0.76$ before and $R = -0.82$, $R^2 = 0.67$ after 2.00 pm local time). Diurnal FQE trends of both photosystems jointly were descending from late morning 9.00 am till afternoon 4.00 pm. A slight late-afternoon increase, observed for three days between 4.00 and 7.00 pm, could be attributed to an increase in FQE of PSI that was retrieved separately from PSII. The method was subsequently extended and applied to airborne SIF images acquired with the HyPlant imaging spectrometer over the same alfalfa field. While the input canopy SIF radiance computed by two different methods, i) a spectral fitting method (SFM) and ii) a spectral fitting method neural network (SFMNN), produce broad and irregularly shaped (skewed) histograms (spatial coefficients of variation: CV = 29–35 % and 14–20 %, respectively), the retrieved HyPlant per-pixel FQE estimates formed significantly narrower and regularly bell-shaped near-Gaussian histograms (CV = 27–34 % and 14–17 %, respectively). The achieved spatial homogeneity of resulting FQE maps confirms successful removal of the TOC SIF radiance confounding impacts. Since our method is based on direct matching of measured and physically modelled canopy SIF radiance, simulated by 3D radiative transfer, it is versatile and transferable to other canopy architectures, including structurally complex canopies such as forest stands.

1. Introduction

Solar-induced chlorophyll fluorescence (SIF) is increasingly exploited as a proxy of photosynthetic functional status of green vegetation. SIF is an electromagnetic radiation emitted by photosystems inside green vegetation leaves that was excited by Photosynthetically Active Radiation (PAR) upon its exposure to solar radiation (Mohammed et al., 2019). It is a subtle photon flux, representing only a small fraction of solar radiation scattered back by vegetation canopies (2–6 % at 740 nm (Campbell et al., 2008)), which is spectrally overlapping with the canopy reflected radiation. Nevertheless, it provides a unique real-time information about the functional state of vegetation photosynthesis, as

* Corresponding author.
E-mail address: oregaieg@uni-bonn.de (O. Regaieg).

https://doi.org/10.1016/j.rse.2025.114636
Received 20 August 2024; Received in revised form 6 January 2025; Accepted 31 January 2025
Available online 5 February 2025

it represents together with photochemical reactions and heat dissipation a possible pathway used by green vegetation to convert and emit part of the absorbed PAR (APAR) energy. In recent years, optical sensors and SIF retrieval techniques from *in-situ* (Cogliati et al., 2015a; Liu et al., 2015; Zhao et al., 2018), airborne (Frankenberg et al., 2018; Rascher et al., 2015; Siegmann et al., 2019) and satellite (Frankenberg et al., 2011; Guanter et al., 2021; Zhao et al., 2024) measurements have been developed. They are exploiting the narrow spectral bands, where SIF has a larger relative contribution to the total radiation scattered by vegetation canopies, such as atmospheric oxygen absorption bands O_2A and O_2B, and the solar Fraunhofer lines. This allowed to harness the remotely sensed SIF for potential applications, such as, vegetation early stress detection (Ač et al., 2015; Song et al., 2018) or tracking vegetation photosynthetic activity and consequent Gross Primary Productivity (GPP) (Guanter et al., 2014; Liu et al., 2019b; Tagliabue et al., 2019; Yang et al., 2021). Yet, the strongest relationship between SIF and photosynthetic activity is found at the spatial scale of the photosystem one (PSI) and the photosystem two (PSII), from where it originates.

The magnitude of emitted SIF radiation is driven by the amount of PAR absorption and the quantum efficiency of fluorescence emission. Before being absorbed in chloroplasts, PAR undergoes wavelength dependent interactions (*i.e.*, scattering and absorption): i) inside the atmosphere, ii) with the vegetation canopy architecture elements, and finally iii) with the anatomical structures of individual leaves. After its emission by PSI and PSII and before its registration by a remote sensing sensor, SIF radiation undergoes the same interactions but in the reverse order, which causes an angular anisotropy of the recorded SIF signal and, to some extent, its decoupling from the plant functional processes (*e.g.*, physiological stress reactions, primary production, *etc.*) (Porcar-Castell et al., 2021). These interactions, undergone by both PAR and SIF radiations, strongly depend on non-physiological confounding factors that are interfering with the photosynthetic activity estimation, such as, the leaf internal structural, biochemical, and optical properties, but also the canopy structure, atmospheric conditions, solar and viewing directions and the actual background (*i.e.*, soil and understory) reflectance (Verrelst et al., 2015). Since the red SIF emission is highly affected by its chlorophyll *a*bsorption, Fournier et al. (2012) found that the red to far-red fluorescence ratio decreased by a factor of two between the leaf and the canopy levels. Therefore, a downscaling, *i.e.*, a normalization, approach is required to reduce (ideally remove) the impacts of the confounding factors and extract information driven purely by photosynthetic processes. Such a downscaling aims at estimating an efficiency of chlorophyll fluorescence at lower spatial scales (*i.e.*, the level of leaf or even the level of photosystems) from radiance measurements acquired at a higher spatial scale (*i.e.*, canopy level). Several canopy-to-leaf SIF downscaling approaches, that were shown to improve the estimation of vegetation GPP (Liu et al., 2020) as well as drought monitoring (Lin et al., 2022), have been proposed.

Yang and van der Tol (2018) approximated the canopy scattering of far-red SIF by a ratio of canopy far-red reflectance to the product of canopy interceptance and leaf albedo. The Fluorescence Correction Vegetation Index (FCVI) was later proposed to overcome the necessity of estimating the canopy interceptance (Yang et al., 2020). Another method, proposed by Zeng et al. (2019), uses the optical index of near-infrared reflectance of vegetation (NIRv) (Badgley et al., 2017), which was found to be more robust against soil effects and, consequently, more applicable for sparse canopies (Bendig et al., 2025). The NIRvH index, utilizing hyperspectral data, was later proposed to further remove residual soil impacts observed in NIRv (Zeng et al., 2021). These methods have the advantage of being simply applicable and, hence, practical. However, they rely on assumptions limiting their performance, *e.g.*, the non-reflective soil assumption for FCVI (Yang et al., 2020) originating from the underlaying spectral invariant theory (Knyazikhin et al., 2011). Additionally, they do not scale the SIF signal all the way down to the photosystems.

More advanced methods, downscaling SIF to the level of PSI and PSII, combine the Soil Canopy Observation, Photochemistry and Energy fluxes (SCOPE) model (van der Tol et al., 2009) with a numerical optimization (Celesti et al., 2018) or with machine learning techniques (Liu et al., 2019a; Scodellaro et al., 2022). Since SCOPE is a one-dimensional (1D) model, the applicability of these approaches is limited to homogeneous and structurally simple canopies. Unlike 1D canopy models, 3D landscape models for SIF radiative transfer work with a more realistic, *i.e.*, spatially heterogenous, canopy structure representation, leading to more accurate top-of-the-canopy (TOC) SIF simulations, especially for architecturally complex multi-species canopies (Malenovský et al., 2021; Regaieg et al., 2021). The Discrete Anisotropic Radiative Transfer (DART) model (Gastellu-Etchegorry et al., 2017) is one of the comprehensive 3D radiative transfer models for optical remote sensing applications. In this study, we used its latest mode called DART-Lux, which was extended to simulate SIF (Regaieg et al., 2023). Being based on the Bi-Directional Path Tracing algorithm (Wang et al., 2022), DART-Lux enhances significantly DART's computational efficiency and delivers superior accuracy compared to the older and traditional Flux Tracking (DART-FT) mode.

The aim of this work is to present and test a new canopy-to-photosystem SIF downscaling method based on the 3D radiative transfer of DART-Lux. This method is, first, applied on *in-situ* diurnal SIF measurements acquired for an alfalfa crop field with a FloX system (Naethe et al., 2024), which allowed us to investigate temporal/diurnal variations of the alfalfa PSI and PSII Fluorescence Quantum Efficiency (FQE). Secondly, the method is adjusted and applied on SIF airborne images recorded by the HyPlant airborne imaging spectrometer (Rascher et al., 2015). This enabled us to produce FQE maps of the alfalfa crop for four dates and assess their spatial variability. The main objective is to demonstrate the potential of 3D DART modeling for extracting a standardized (*i.e.*, SIF efficiency comparable among different observations, spatial and temporal scales, canopy structures, and atmospheric conditions, *etc.*) photosystem-level physiological information from temporally resolved and spatially explicit TOC SIF radiance measurements. The study addresses the following two research questions: 1) how does the retrieved FQE vary diurnally and is this variation in accordance with published diurnal courses of crop photosynthetic activities, and 2) how does the FQE retrieved from airborne SIF imagery vary spatially in comparison to the spatial variation of TOC SIF radiance?

2. Materials and methods

2.1. Data acquisition and preprocessing

2.1.1. Study site

The study was conducted in a mono-species agricultural field of an alfalfa (*Medicago sativa*) crop, located northeast of the city of Lleida (Catalonia, Spain) (Appendix A). The data acquisition was carried out during the Land surface Interactions with the Atmosphere over the Iberian Semi-arid Environment (LIAISE) measurements campaign, in summer 2021.

2.1.2. In-situ SIF data

The collected data includes diurnal measurements acquired with a FloX system (JB Hyperspectral Devices GmbH, Germany). The FloX system measures spectrally resolved TOC upwelling (25° field-of-view (FOV)) and solar downwelling radiance (180° FOV). It has two spectrometers. 1) FLAME (Ocean Optics, USA): a Visible – Near Infrared (400–950 nm) spectrometer with 0.65 nm Spectral Sampling Interval (SSI) and a spectral resolution of 1.5 nm Full Width at Half Maximum (FWHM). 2) QE Pro (Ocean Optics, USA): a fluorescence spectrometer (650–800 nm) with 0.17 nm SSI and a spectral resolution of 0.3 nm FWHM. The nadir viewing bundle of FloX optical fibers was positioned at 2 m high, which corresponds to a circular measurement footprint of c. 0.9 m in diameter on the ground.

The standard FloX processing, provided by the FloX manufacturer, was applied to the recorded dataset to convert raw data to at-sensor radiance. In the next step, the SFM algorithm was employed to retrieve SIF from the O_2A and O_2B oxygen absorption features at 760 and 687 nm and the SpecFit algorithm was applied to reconstruct the full SIF radiance spectrum for each measurement. More details about the SFM and the SpecFit method can be found in Cogliati et al. (2015b) and Cogliati et al. (2019), respectively. In this study, we used the local maximum of the red SIF peak (around 685 nm) and the far-red peak (around 740 nm) computed from the fully reconstructed SIF radiance spectra. We analyzed FloX observations acquired on six consecutive days between 17th and 22nd of July 2021. To reduce the noise originating from the high temporal frequency of one-minute full SIF spectra retrieved from the FloX measurements, we aggregated the values into 15-min steps by averaging the measurements over ten-minute windows centered around each 15-min step.

Figure 1 shows the diurnal variation of the SIF radiance at the red and the far-red peaks.

The incoming broadband PAR radiation [400–700 nm] was measured using a Kipp&Zonnen PAR Lite sensor. Figure 2 shows the diurnal PAR for the six days of interest from 17th to 22nd July 2021.

2.1.3. Optical properties

ASD Fieldspec-4 spectroradiometer (Malvern Panalytical Ltd., USA), equipped with an ASD leaf-clip and a pistol grip, was used to collect optical properties of leaf and soil reflectance samples on 19th and 20th of July 2021.

2.1.4. Active measurements of PSII photosynthetic yield

To get further insight in the relationship between retrieved FQE values and the actual photosynthetic activity, the photosynthetic yield of PSII was measured with a miniaturized pulse-amplitude modulated photosynthesis yield analyzer (Mini-PAM) (Bilger et al., 1995). The PSII photosynthetic yield was calculated as (Fm' − F)/Fm', where F is the fluorescence yield of a light-adapted leaf and Fm' is its maximum fluorescence yield after exposure to a saturation light pulse. These measurements were done on 19th July 2021. Since the canopy was still open on that day, leaves were predominantly sunlit and, hence, the measured TOC SIF originated mostly from the sunlit leaves. Ten sets of sunlit leaves were measured during that day. Each set was composed of 17 to 30 sample leaves, which were measured within a time interval of 10 to 25 min. The measured quantities of every set were averaged and associated to the middle point of the corresponding measuring time interval.

2.1.5. Airborne SIF images

For spatial analyses, we used imaging data of the HyPlant airborne instrument that was specifically designed for vegetation monitoring and SIF retrieval. It contains a DUAL imaging spectrometer, measuring surface reflectance in the spectral range from 380 to 2500 nm, and a FLUO imaging spectrometer with a distinctly higher spectral resolution and FWHM within the 670–780 nm spectral range for retrieval of SIF (Rascher et al., 2015; Siegmann et al., 2019). During the six days considered in this study, four HyPlant overflights were performed: 1) on 17th July at 2:00 pm, 2) on 20th July at 3:32 pm, 3) on 21st July at 3:42 pm and 4) on 22nd July at 2:04 pm (local time), providing images with a ground sampling distance of 1.7 m.

Two different retrieval methods were applied to the HyPlant FLUO data to derive TOC SIF from the O_2A absorption band (Fig. 3, Fig. 4): i) the Spectral Fitting Method (SFM) (Cogliati et al., 2019), and ii) the Spectral Fitting Method Neural Network (SFMNN) (Buffat et al., 2025) method, which is a novel, self-supervised, neural network-based adaption of SFM. Similarly to SFM, it aims at disentangling the at-sensor signal recorded by an imaging spectroradiometer through fitting a simplified physical model of at-sensor radiance. The model encompasses i) the parameterization of surface properties such as reflectance and fluorescence spectral forms, ii) the down and upwelling radiative transfer through the atmosphere, and iii) the sensor response affected by miscalibration of the at-sensor signal. While the fit in SFM is performed for each observed pixel individually by means of a least-squares optimization, SFMNN trains a neural network that learns features in the spectral input to optimally reconstruct the measured at-sensor radiance. SFMNN leverages physical, signal and sensor-specific properties to invert the radiative transfer that yields the measured at-sensor radiance. Since this inversion is ill-posed its reconstruction-based loss formulation has to be extended by multiple constraining regularizers and an architectural constraint. At its core, SFMNN trains an encoder-decoder type of

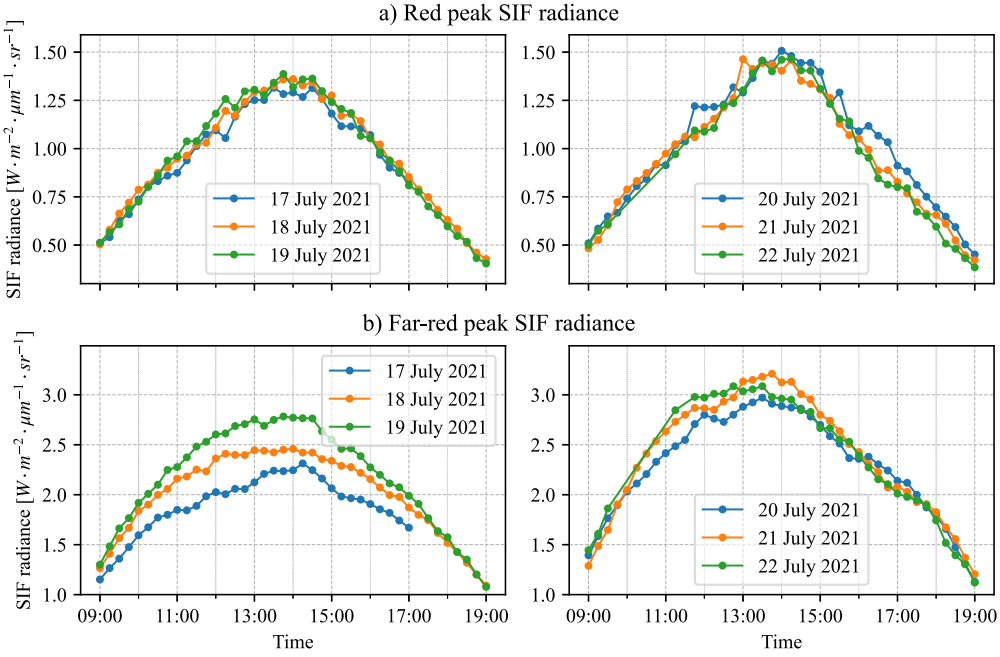

Fig. 1. Diurnal courses of FloX measured SIF radiance at the red peak (a) and at the far-red peak (b) computed using the specFit method. (For interpretation of the references to color in this figure legend, the reader is referred to the web version of this article.)

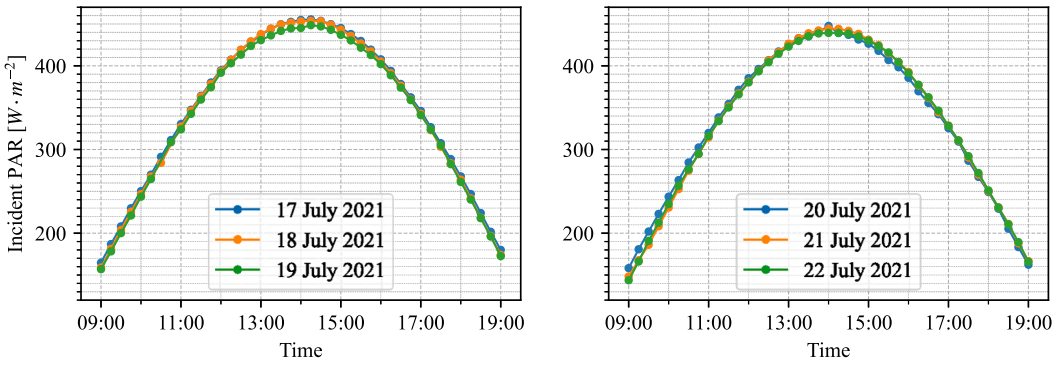

Fig. 2. Diurnal courses of incident photosynthetically active radiation (PAR [400–700 nm]) for six days from 17th to 22nd July 2021.

architecture. It is based on multi-layer perceptrons predicting the physical variables that parameterize the signal generation model within individual image patches of a fixed size. It differentiates between a pixelwise and a patch-wise prediction, where patch-wise variables are estimated as single scalars for individual patches. This differentiation in output dimensionality mirrors the difference in spatial auto-correlation of the trained model components. As a consequence, variables related, *e.g.*, to the surface reflectance and SIF emission are predicted in a pixel-wise fashion, while the atmospheric transfer is estimated on a patch-wise basis. No labeling is used during the self-supervised training of SFMNN. The loss adopted for SFMNN consists of a weighted reconstruction residual with two additional regulators ensuring physiological and physical plausibility of the retrieved SIF. The reconstruction residual imposes implicit constraints on the network optimization. The spectral weighting used in this loss part reflects varying SIF signal strength in the spectral dimension according to actual SIF signal and sensor characteristics. Additionally, the physiological regulator forces SFMNN to predict vanishing fluorescence emission in barren image pixels, while the physical regularization ensures that the predicted atmospheric transfer corresponds to a normalized function with an upper boundary. The SFMNN can be in principle formulated for various data acquired by a range of different hyperspectral imaging sensors. In a validation study, in which SFMNN results were compared to *in-situ* SIF estimates, Buffat et al. (2025) found comparable prediction performances of both SFMNN and SFM methods when applied to HyPlant FLUO data within a validation study using *in-situ* TOC SIF measurements from multiple years. Yet, some significant differences in the SIF predictions between the two methods occured. Subsequently, the authors found a lower prediction noise and improved correlation scores of SFMNN but also a systematic overestimating bias with respect to the *in-situ* SIF measurements. Certain uncertainties in the assessment of performance remain, due to a large performance variation across data sets possibly due to disregarding directional effects in the validation.

2.2. Downscaling methodology

2.2.1. Generalized method

The SIF downscaling is done in the four steps aiming to estimate the photosystem-level FQE:

- *Irradiance inversion*

The incoming PAR is inverted using the DART atmospheric radiative transfer module to compute atmospheric optical depth (AOD) by matching a simulated PAR to the measured one (Wang et al., 2020). The retrieved AOD values are subsequently used as inputs in DART atmospheric radiative transfer, allowing for a sufficiently representative division between direct and diffuse spectral irradiance within the PAR region (see an example in Appendix B). This division is important for correct induction of DART-modelled SIF emissions.

- *Optical properties definition*

Measured soil reflectance spectra are directly imported in DART, whereas leaf optical properties are modelled with the Fluspect-Cx model (Vilfan et al., 2018), using the leaf structural number N, leaf contents of chlorophylls, carotenoids, anthocyanin pigments, and dry matter as input parameters. These parameters can be estimated either by inverting the Fluspect-Cx model based on leaf-level optical properties measurements, or by inverting DART coupled with Fluspect based on canopy-level reflectance measurements. The leaf water content is not relevant for this study since the spectral range of its absorption is outside the SIF excitation and emission ranges.

- *3D mock-up creation*

Two 3D computer representations of alfalfa plants, required for 3D radiative transfer, were created in the Blender software (https://www.blender.org) according to multi-angular photographs of the actual plants takenin the field against a white background used as backdrop in Blender (see screenshots from Blender provided in the supplementary materials). Based on information about canopy structure derived from different available sources, such as high-resolution RGB photos, spectroradiometer TOC reflectance measurements, multi/hyperspectral imagery, a representative 3D mock-up of the alfalfa field is created.

- *FQE estimation*

In this step, a DART simulation is run to produce TOC SIF radiance using a reference value of FQE as a first guess. Then, the estimated FQE value is inferred from the measurement and, in the case of SIF images, from the simulated TOC SIF radiance with potentially additional simulations.

2.2.2. Application to FloX in-situ diurnal measurements

- *Optical properties definition*

Since the ASD leaf-clip does not allow to directly measure leaf transmittance, we complemented the measured leaf reflectance with the simulated transmittance by retrieving its input properties through the inversion of the Fluspect-Cx model (Vilfan et al., 2018). The model inversion was done in two consecutive steps: i) retrieval of the leaf structural coefficient N using the maximal reflectance within the near-infrared plateau (750–850 nm) by adapting a method published in Jacquemoud et al. (1996), and ii) cascading retrieval of the leaf biochemical properties (*i.e.*, chlorophyll a + b, total carotenoid, anthocyanin, water, and dry matter contents) as described in Malenovský et al. (2006) and Lamsal et al. (2022). The retrieved leaf structural and biochemical properties of 43 measured leaves were averaged and used as Fluspect-Cx inputs to simulate leaf spectral

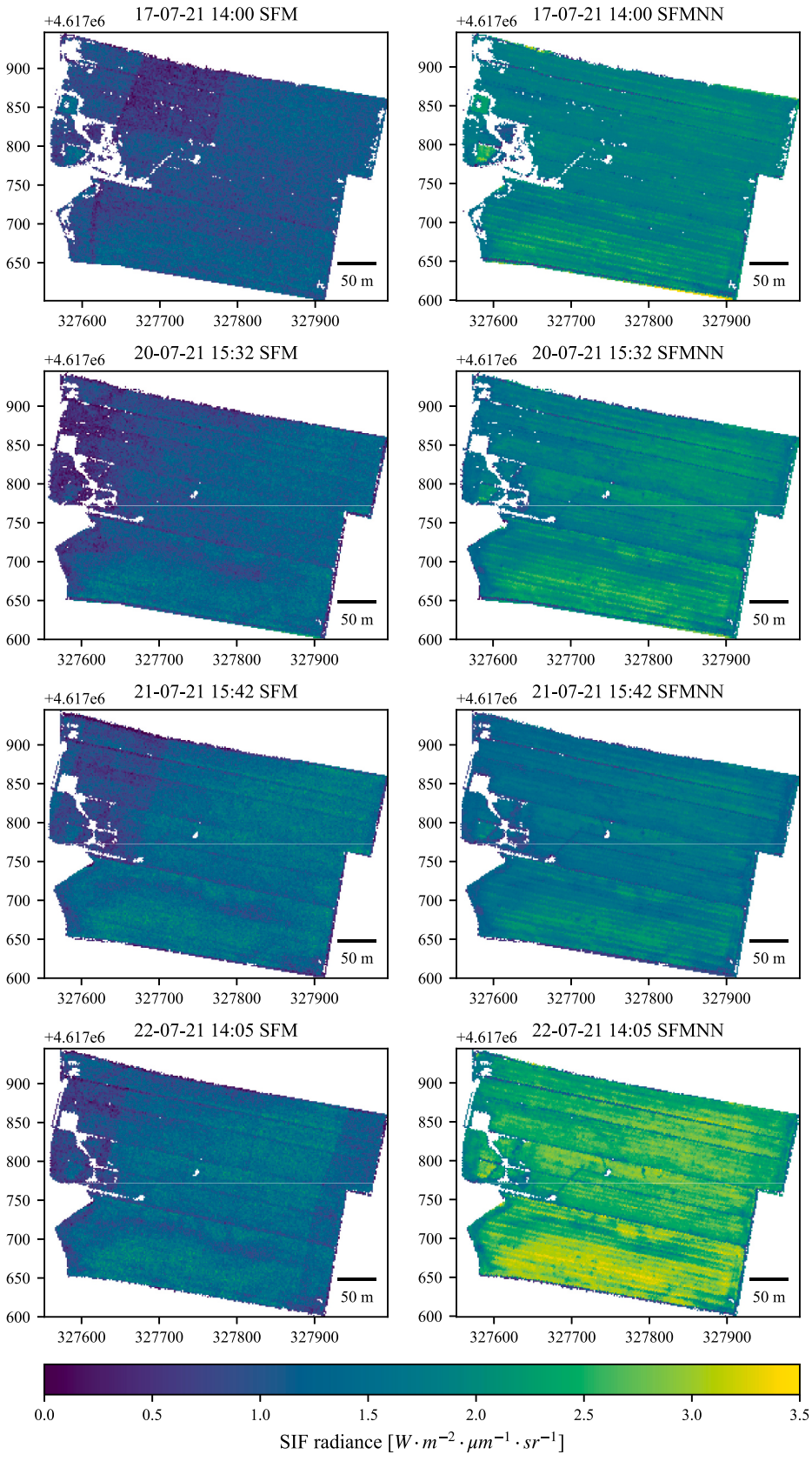

Fig. 3. SIF O_2A radiance images at the top of observed alfalfa canopy derived from four HyPlant overflights using the SFM (left) and the SFMNN (right) methods.

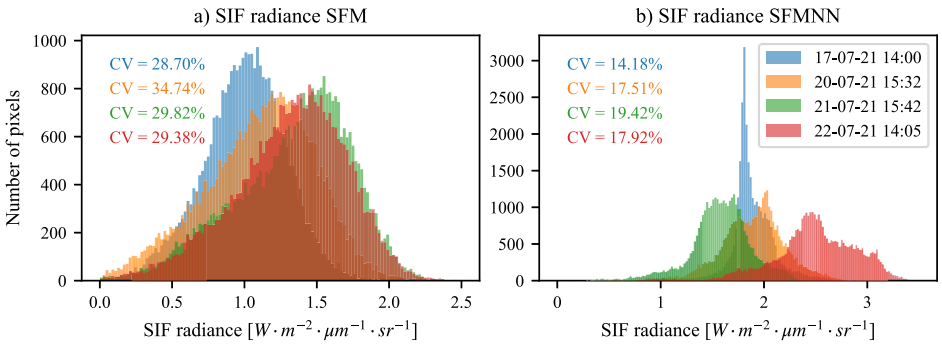

Fig. 4. Histograms and coefficients of variation (CV) of the top-of-the-canopy SIF radiance images for the four HyPlant overflights retrieved with the SFM (a) and the SFMNN (b) methods.

reflectance, transmittance, and subsequently also fluorescence excitation-emission matrices.

- *3D mock-up creation*

Created 3D objects of differently high and large plants were manually positioned and scaled to approximate the photos taken by a RGB camera, depicting the field of view of the FloX optical fibers on the top of the crop canopy. This way, we created six 3D mock-ups for the six investigated days (*i.e.*, 17th to 22nd July 2021). Fig. 5 illustrates the RGB photos and the corresponding DART-simulated RGB images for these six days. Fig. 6 shows a comparison between the TOC reflectance measured by FloX and simulated by DART on 19th July 2021 at 10 am (local time) as an example.

- *Diurnal FQE estimation*

The FQE retrieval is done using a single forward DART simulation of the top-of-canopy SIF radiance using as input an arbitrary FQE value. The coefficients of the SIF excitation-emission matrices, computed by the Fluspect-CX leaf fluorescence model (Vilfan et al., 2018) embedded in DART, increase proportionally with the increase of FQE representing

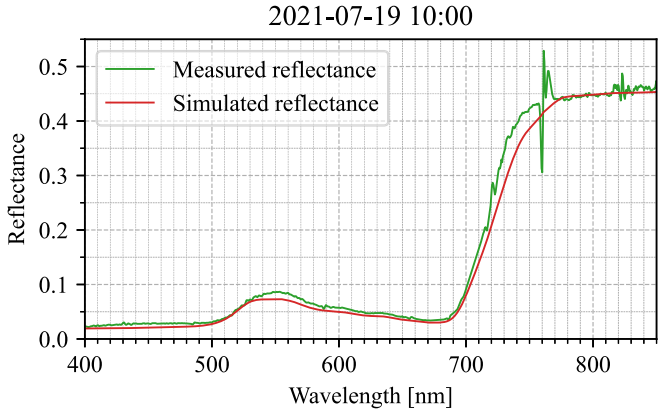

Fig. 6. FloX-measured and the corresponding DART-simulated top of canopy reflectance (19th July 2021, 10 am local time).

both photosystems, while keeping all leaf biochemical properties fixed as retrieved from *in-situ* measured leaf optical properties (described above). Consequently, the first order TOC SIF emission (*i.e.*, SIF induced

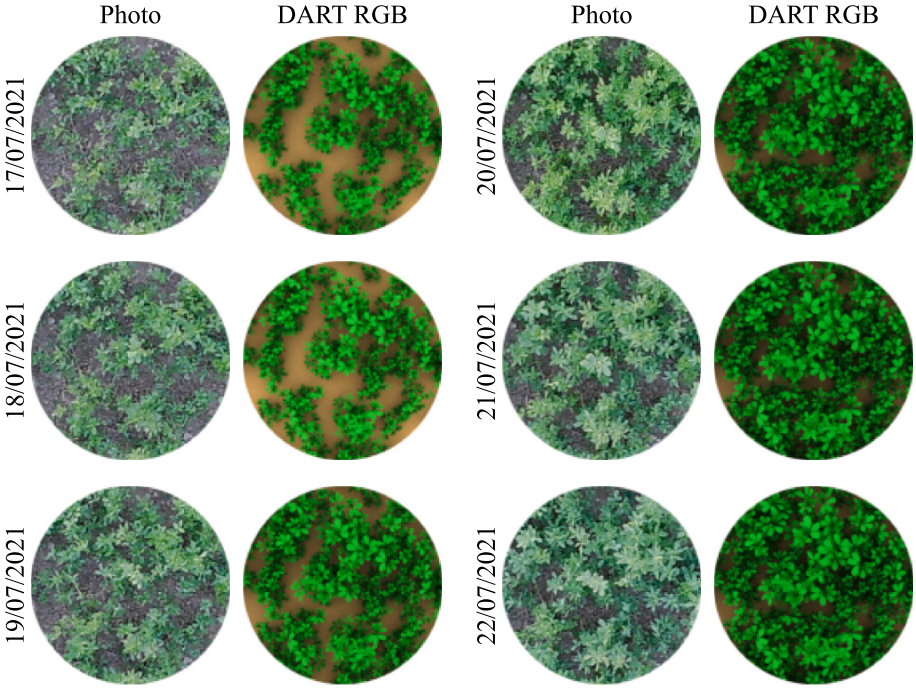

Fig. 5. RGB camera photos and DART simulated RGB images over the field of view of the FloX system for the six considered days.

by previously computed direct and diffuse solar irradiance, which was intercepted by a leaf directly and after being scattered by canopy elements) also increases proportionally to the FQE magnitude. Higher order TOC SIF emissions (*i.e.*, SIF induced by re-interception of the previously emitted SIF radiation) are proportional to the n^{th} power of FQE, with n being the order of emission. Since the FQE is significantly smaller than one, these higher order SIF emissions are, in practice, very small compared to the first order SIF emission. Additionally, the propagation of SIF radiation through the canopy is not influenced by the FQE values. Thus, the TOC SIF emission can be assumed to increase proportionally to the increase in FQE, if all other scene (*i.e.*, crop field) parameters are held constant.

Accepting this assumption, one can consider the arbitrary FQE value as the reference (FQE_{ref}) and compute an estimation of the FQE value (FQE_{est}) ensuring the equality of simulated and measured TOC SIF radiance as follows:

$$FQE_{est} = FQE_{ref} \bullet \frac{SIF_{meas}}{SIF_{ref}} \quad (1)$$

where FQE_{ref} is the reference FQE value used for the forward DART simulation, SIF_{ref} is the TOC SIF radiance simulated using FQE_{ref}, and SIF_{meas} is the measured TOC SIF radiance.

Eq. (1) can be used to estimate FQE from SIF radiance measured at any spectral band (*e.g.*, O_2A or O_2B absorption features) of a spectrally resolved SIF radiance.

In this study, we target the maximum of the SIF radiance at the far-red SIF peak around 740 nm, allowing for a good agreement between the simulated and the measured SIF values regardless of a spectral wavelength shift (see Fig. 7.a).

This estimation method was modified to estimate also FQEs of PSI and PSII separately by employing an older version of the Fluspect-CX model (Vilfan et al., 2016). Considering that red SIF is associated mainly with PSII and far-red SIF is emitted by both PSI and PSII (Franck et al., 2002; Iriel et al., 2014; Porcar-Castell et al., 2021), the estimation of the PSI and PSII FQEs was computed as follows:

i. First forward DART simulation of TOC SIF with FQE reference values for PSI and PSII ($FQE_{ref,PSI}$ and $FQE_{ref,PSII}$, respectively).
ii. Estimation of FQE for PSII ($FQE_{est,PSII}$) based on the red peak of measured SIF radiance ($SIF_{meas,red}$) and the red peak of the simulated PSII SIF radiance ($SIF_{ref,red,PSII}$):

$$FQE_{est,PSII} = FQE_{ref,PSII} \bullet \frac{SIF_{meas,red}}{SIF_{ref,red,PSII}} \quad (2)$$

Second forward DART simulation parametrized with the $FQE_{ref,PSI}$ and $FQE_{est,PSII}$ values

iii. Estimation of FQE for PSI based on the far-red peak of the measured TOC SIF radiance ($SIF_{meas,far-red}$), the far-red peak of the simulated PSI SIF radiance ($SIF_{sim,far-red,PSI}$), and the far-red peak of the simulated PSII SIF radiance ($SIF_{sim,far-red,PSII}$):

$$FQE_{est,PSI} = FQE_{ref,PSI} \bullet \frac{SIF_{meas,far-red} - SIF_{sim,far-red,PSII}}{SIF_{sim,far-red,PSI}} \quad (3)$$

The DART SIF radiance simulated with the estimated $FQE_{est,PSI}$ and $FQE_{est,PSII}$ values allowed for finding a close agreement between simulated and measured SIF spectra (see Fig. 7.b).

2.2.3. Application to HyPlant airborne measurements

- *Preliminary step: a sensitivity analysis assessing canopy structural impacts*

To investigate the potential impact of vegetation canopy structure within the newly proposed FQE estimating approach and to identify the most influential structural parameters, the FQE estimation from FloX was additionally applied to the following specific canopy representations:

i. One-dimensional (1D) mock-ups represented by a quasi-turbid medium (*i.e.*, a cloud of very small leaf facets approximating a foliage turbid medium) with the same Leaf Area Index (LAI) and Leaf Angular Distribution (LAD) as the original canopy mock-ups,
ii. 3D mock-ups of randomly distributed reconstructed alfalfa plants with the same LAI and LAD as the original canopy mock-ups.
iii. 3D mock-ups of randomly distributed reconstructed alfalfa plants with the same canopy cover fraction as the original canopy mock-ups, and

- *Retrieval of canopy traits for optical properties definition and 3D mock-up creation*

To perform the FQE retrieval from HyPlant SIF image data, a reality representing mock-up must be created and parametrized for the whole alfalfa field. Since the manual 3D mock-up construction of a large-sized crop field is unfeasible, we retrieved the actual per-pixel leaf biochemical properties (*i.e.*, the Fluspect-CX inputs) and the canopy cover fraction from HyPlant hyperspectral reflectance images of the same canopy.

For each analyzed HyPlant overflight, a look-up table (LUT) of simulated HyPlant hyperspectral reflectance signatures associated to their respective input parameters were simulated in DART for small 1 × 1 m^2 scenes, with randomly distributed plants. Table 1 shows the DART input parameters used to generate the reflectance LUT. Since

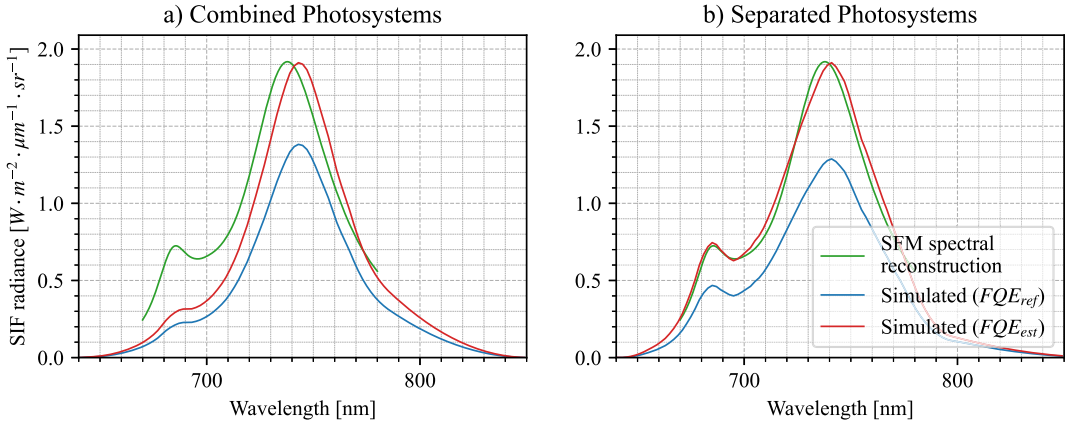

Fig. 7. Spectral reconstruction of measured TOC SIF radiance in comparison to DART TOC SIF radiance simulated using reference FQE values (FQE_{ref}) and estimated FQE values (FQE_{est}) for a) combined photosystems, b) PSI and PSII separately on 19th July 2021 at 10 am (local time).

Table 1
DART input parameters for simulation of HyPlant-like reflectance look-up table.

Parameter	Min value	Max value	Step
Structural coefficient N	2	2.2	0.05
Chlorophyll content [$\mu g \bullet cm^{-2}$]	20	80	10
Carotenoid content [$\mu g \bullet cm^{-2}$]	5	15	2
Dry matter content [$g \bullet cm^{-2}$]	0.002	0.02	0.003
Anthocyanin content [$\mu g \bullet cm^{-2}$]	0	7	1
Canopy cover fraction	0.0538	0.9527	~0.05

wavelengths impacted by absorption of leaf water are not simulated, the leaf water content was kept as a default Fluspect-CX value. Field-measured reflectance of two soil spectra (*i.e.*, dark and bright) and their arithmetic average (spectra shown in Appendix C) were used in the DART simulations to consider the spatial variability in soil reflectance. The generated LUT was used to train Artificial Neural Network (ANN) models that were, subsequently, applied per HyPlant image pixel to estimate the targeted leaf and canopy traits (*i.e.*, leaf structural number N, leaf contents of chlorophyll, carotenoid, and anthocyanin pigments, dry matter content, and canopy cover fraction). The ANNs produced, in addition, a soil coefficient between 0 and 1 per pixel (Fig. E2), which was used to compute a weighted average of the dark and the bright soil reflectance spectra (*i.e.*, 0: dark soil, 1: bright soil, 0.5: averaged soil). Feedforward ANNs with different architectures (one and two hidden layers, varying number of neurons per layer), different activations functions (*i.e.*, ReLu, tanh, and sigmoid) were trained for different number of epochs (1 to 10 epochs). The best estimation among the tested ANNs was chosen based on Root Mean Square Error (RMSE) calculated between the HyPlant and the DART simulated reflectance signatures within the spectral range of 450 to 850 nm. The pixels corresponding to the neighboring fields, as well as the pixels with values of Normalized Difference Vegetation Index (NDVI) < 0.4, corresponding to tractor tracks within and around the field, were excluded from the comparison.

- *3D mock-up creation and parametrization*

The DART 3D mock-up was created and parametrized per HyPlant pixel automatically through a Python script HyPlant SIF. The estimated leaf/canopy traits and soil coefficients were used as input parameters. The method used for building the DART mock-up for the whole alfalfa field is described in Appendix D.

- *FQE estimation:*

The DART 3D mock-ups constructed for every HyPlant pixel, were used to run forward DART SIF simulations based on a reference FQE value that was spatially constant over the whole analyzed field. Unfortunately, the proportionality assumption of the TOC SIF radiance in HyPlant images to the simulated FQE became less accurate, as the SIF value of a given HyPlant pixel was impacted by the values of its neighboring pixels through the scattering of the SIF emitted in the neighboring pixels by the plants and, eventually, the bare soil in a given pixel (*i.e.*, the adjacency effect). Therefore, more than one FQE adjustment iteration was needed to find a good agreement between the DART simulated and the HyPlant acquired SIF images. The best fitting per-pixel FQE was found as follows:

i. Iteration 0:
   - o Forward simulation of TOC SIF radiance ($SIF_{DART,0}$) using a reference value FQE_0 constant over the field
   - o First adjustment of the FQE value per pixel (x, y) :

$$FQE_1(x,y) = FQE_0 \bullet \frac{SIF_{HyPlant}(x,y)}{SIF_{DART,0}\ (x,y)} \tag{4}$$

ii. Iterations $i > 0$:

while $RMSE\left(SIF_{DART,i-1}, SIF_{Hyplant}\right) > \varepsilon = 0.01\ W \bullet m^{-2} \bullet \mu m^{-1} \bullet sr^{-1}$:

- o Simulation of TOC SIF radiance ($SIF_{DART,i}$) using the adjusted $FQE_i(x,y)$. The impact of the neighboring pixels' FQE on the pixel (x,y) SIF radiance is intrinsically accounted for by DART
- o Adjustment of the FQE value per pixel (x,y) :

$$FQE_{i+1}(xy) = FQE_i(xy) \bullet \frac{SIF_{HyPlant}(xy)}{SIF_{DART,i}\ (xy)} \tag{5}$$

3. Results

3.1. FloX diurnal measurements

- *Diurnal FQE retrieval*

Fig. 8 shows the diurnal courses of retrieved FQE values for the six days considered in this study. The diurnal variation trend is similar but not the same; FQE decreased from the morning hours until around 4:00 pm. After this time, it remained constant for first three days, while it increased again in last three days, showing a local maximum around 6:00 pm.

Fig. 9 shows FQE diurnal courses during the six analyzed days retrieved for PSI and PSII separately. Somewhat similar trends are observed in these diurnal courses; the FQE decreased from morning to afternoon hours, with a recovery after 4 pm in the case of PSI and with a small rise for PSII around the solar noon. It is worth noting, that these diurnal courses are impacted by a higher noise, originating mainly from the quality of red SIF radiance measurements.

- *Structural canopy parameters relevant for spatial retrieval of FQE*

Fig. 10 illustrates how the FQE values retrieved using a one-dimensional (1D) representations of alfalfa canopy were systematically underestimated when compared to the FQE values retrieved using geometrically precise (realistic) 3D mock-ups. The FQE estimates resulted in higher relative RMSE for earlier growth stages (18th of July 2021), when the canopy had more air gaps due to a lower LAI and a smaller canopy cover fraction.

Fig. 11 shows FQE values of three selected days retrieved using DART mock-ups with randomly distributed 3D plants but of the same LAI (top row) and of the same canopy cover (bottom row) as the original realistic mock-ups. The FQEs are overestimated for the first case (relative RMSE being nearly constant for the three growth stages), whereas they are nearly identical to FQEs retrieved using realistic mock-ups for the second case. Thus, the correct parametrization of the alfalfa canopy cover fraction was found to be more crucial for an accurate FQE retrieval than parametrization of its LAI.

3.2. HyPlant airborne measurements

- *Retrieved leaf/canopy traits and DART simulations of TOC reflectance image*

The ANN-based retrievals of leaf, canopy, and soil properties (see example in Appendix E) allowed for a genuine, spatially explicit, per-pixel, biochemical and structural parametrization of the observed alfalfa field (c.f., true-color images of the HyPlant acquisition and the DART simulation for 22nd July 2021 in Fig. 12). The average hyperspectral reflectance signatures and the complementary standard deviations of the whole alfalfa field as acquired by the HyPlant Dual imaging spectrometer and simulated by DART are depicted in Fig. 13.

- *Retrieved FQE maps*

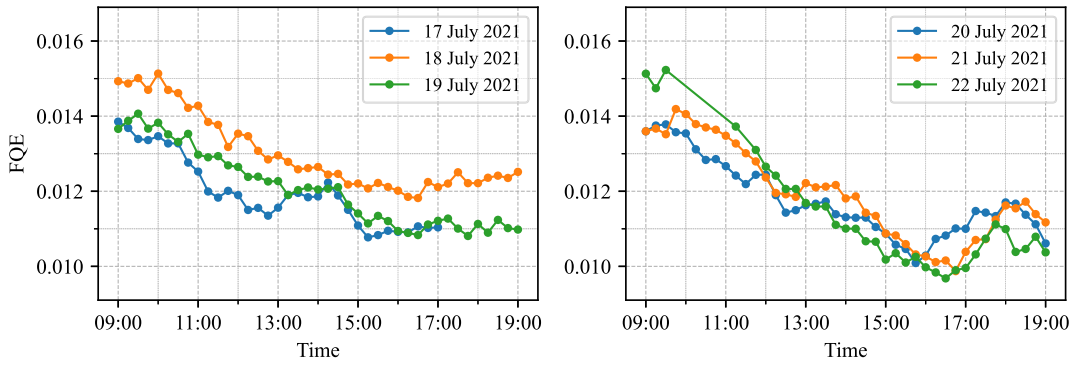

Fig. 8. Diurnal variations of combined PSI and PSII FQE, retrieved from FloX measurements acquired during six analyzed days (left: first three days (open canopy); right: last three days (closed canopy)).

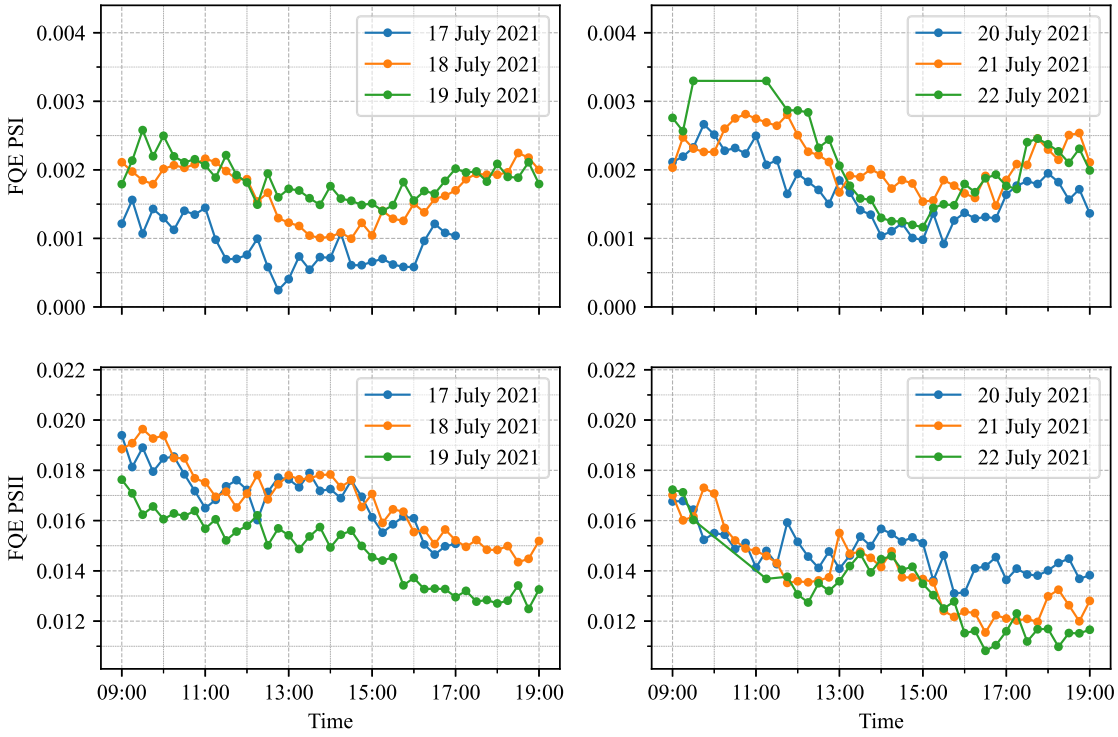

Fig. 9. Diurnal variation of PSI and PSII FQE, retrieved separately from FloX measurements acquired during the six analyzed days (left: first three days (open canopy); right: last three days (closed canopy)).

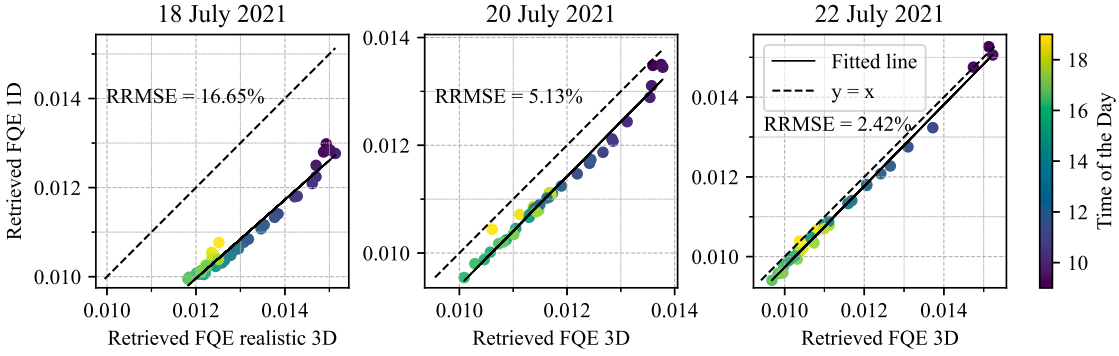

Fig. 10. Comparison of FQE values retrieved for three example days using realistic 3D and equivalent 1D mock-ups of the alfalfa crop.

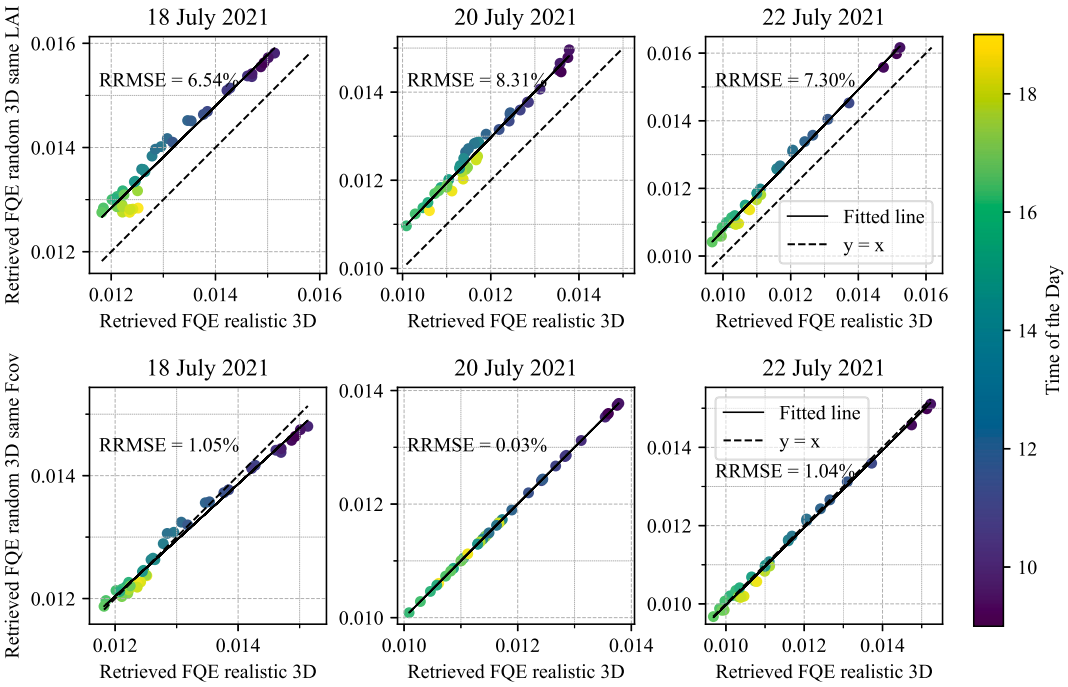

Fig. 11. Comparison between the FQE retrieved using realistic 3D and randomly distributed 3D mock-ups with the same LAI (top) and with the same canopy cover fraction (Fcov) (bottom).

The method in paragraph 2.2.3 allowed for finding a close agreement between the DART simulated TOC SIF radiance and the HyPlant SIF radiance images. Two examples from SFM and SFMNN are shown in Appendix F. Fig. 14 presents the maps of FQE values for both PSI and PSII together, retrieved using the TOC SIF radiance produced by SFM and SFMNN, while Fig. 15 depicts their respective histograms for four HyPlant acquisitions captured on 17th, 20th, 21st, and 22nd July 2021. Visually, one can say that the FQE maps of SFM inherited the noise and the artefacts of the input TOC SIF radiance maps, while FQE based on SFMNN is spatially more consistent, as it inherited a less noisy spatial pattern. Due to imperfect spatial co-registration between hyperspectral reflectance and SIF images, few outlying FQE values appeared, especially at borders of the alfalfa field. These outliers were removed based on thresholds of their z-score ($z > 6\sigma$, with σ the standard deviation of the FQE map) for plotting the histograms and computing the coefficient of variation (CV).

Finally, Fig. 16 shows scatterplots between SFM and SFMNN TOC SIF radiance and their corresponding retrieved FQE values for the same four HyPlant overflights.

4. Discussion

4.1. Removed impact of confounding factors

The temporal (diurnal) and spatial (local) variations of the steady-state, light-adapted FQE at the level of photosystems were successfully retrieved for an alfalfa crop. Similarly to previous studies (*e.g.*, Amoros-Lopez et al., 2008; Hu et al., 2023), the diurnal variation of TOC SIF radiance (Figure *1*) was found to be driven mainly by the PAR diurnal variation (Figure *2*). Our downscaling approach, using DART-Lux 3D radiative transfer (Wang et al., 2022) simulating TOC SIF (Regaieg et al., 2023), allowed us to extract the physiological part of SIF signal. The physical modeling of SIF (*i.e.*, 3D induction by APAR, emission by photosystems and leaves, and propagation through canopy) removed the impact of confounding factors, specifically, spatiotemporally changing intensity of PAR, complex canopy architecture combined with changes in sun-canopy-sensor geometry, as well as SIF absorption and scattering by plant leaves, stems, and bare soil beneath them. This is obvious when comparing maps of TOC SIF and FQE, retrieved from HyPlant observations. While the canopy SIF radiance (Fig. 3) is spatially varying, the spatial pattern of FQE (Fig. 14) is homogeneous, suggesting a spatially uniform photosynthetic performance of plants of the investigated alfalfa variety. Geometrically regular patches of spatially varying FQE retrieved from the SFM product were inherited from the SFM computation of SIF radiance (c.f. left columns of Fig. 3 and Fig. 14), and not caused by the environmental and canopy confounding factors. The comparison of TOC SIF radiance histograms (Fig. 4) with FQE histograms after SIF downscaling (Fig. 15) revealed narrower and more bell-shaped Gaussian distributions due to the minimized impact of canopy confounding factors. Additionally, the coefficient of variation (CV) of FQE estimates was lower than CV of SIF TOC radiance for the HyPlant overflights on 20th, 21st and 22nd July. This was not the case in the dataset recorded on 17th July, which corresponds to an earlier growth stage (*i.e.*, a lower canopy cover fraction), where the SIF radiance CV was lowest due to the bare soil impact. On the one hand, it seems that the effect of our SIF downscaling is less pronounced in results of the SFM method, as its SIF TOC radiance CV was already high, and histogram was bell-shaped (Fig. 4). This can be explained by a higher spatial noise of the SFM SIF radiance (see Fig. 3). Since SFMNN produced a less noisy and more spatially consistent distribution of TOC SIF radiance, its FQE maps show, compared to the SFM FQEs, no spatial artefacts. On the other hand, systematically higher values of TOC SIF radiance found for the SFMNN method were also propagated to the FQE estimates. The relative differences between the SFM and SFMNN SIF radiances and their FQE estimates were found to have similar proportions, which might be explained by their near-linear relationships, and is shown in Appendix G.

4.2. Impact of the canopy structure representation

Our canopy structure sensitivity analysis showed that use of 1D instead of 3D crop representations resulted in an underestimation of FQE (Fig. 10). The underestimation is a direct consequence of the TOC SIF radiance overestimation, caused by neglection of foliage shadowing,

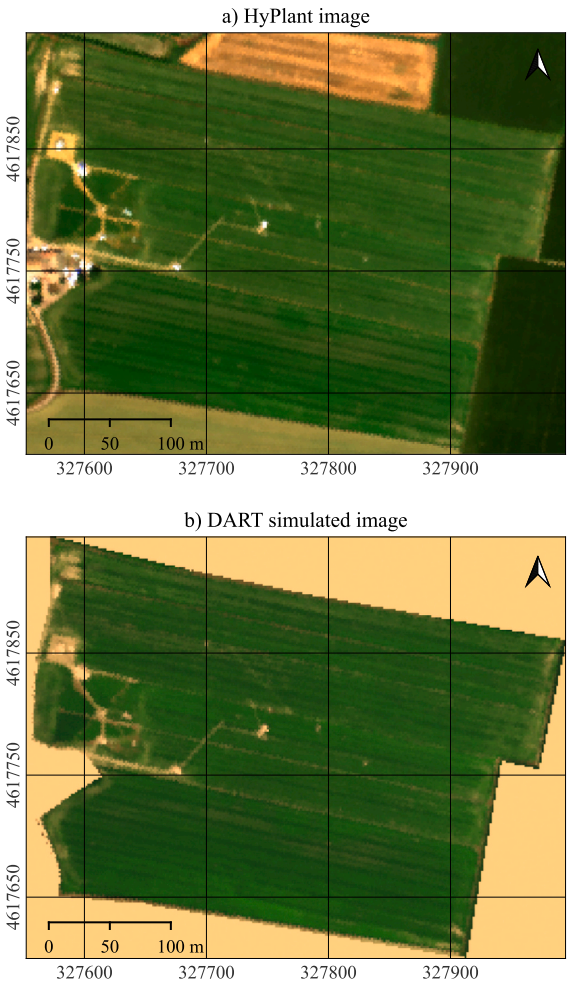

Fig. 12. True color composites for the alfalfa field sensed by the HyPlant Dual hyperspectral sensor during the overflight on 22nd July 2021 (a) and simulated by DART-Lux (b), using the scene parameters retrieved from the hyperspectral image.

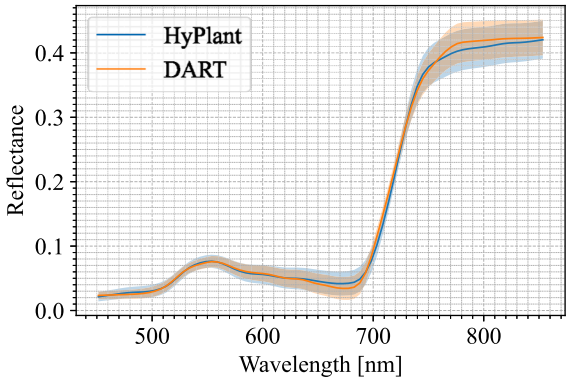

Fig. 13. Mean reflectance signatures (± standard deviation (shaded areas)) extracted from HyPlant acquisition and corresponding DART simulation of the investigated alfalfa crop field pixels on 22nd July 2021.

clumping, and missing canopy gaps exposing bare soil. This leads to overestimations of both the PAR absorption by plants and the canopy SIF escape (Boitard et al., 2023; Malenovský et al., 2021; Regaieg et al., 2021). The FQE underestimation was more pronounced in earlier growth stages that are characterized by a lower canopy cover fraction. Since bare soil does not emit SIF and only scatters SIF radiation

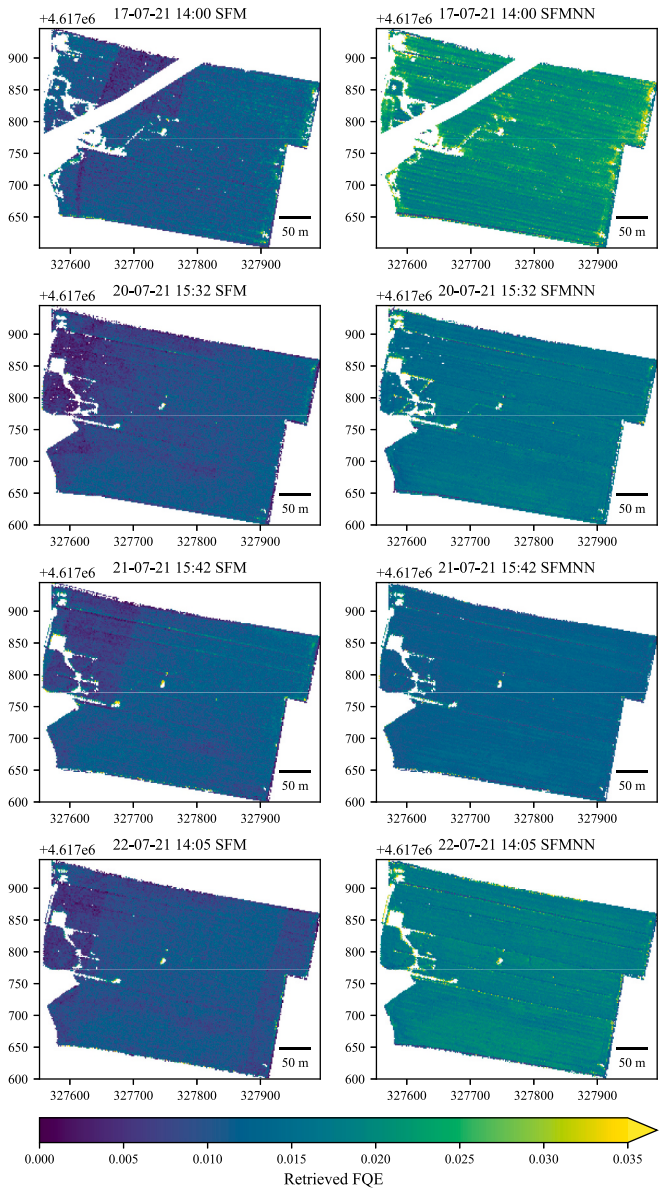

Fig. 14. FQE maps derived from HyPlant SFM (left column) and SFMNN (right column) retrieved TOC SIF radiance data, acquired on 17th, 20th, 21st, and 22nd July 2021.

originating from the leaves, its contribution to total at-sensor SIF radiance is, compared to vegetation, much lower. Consequently, the DART canopy SIF radiance simulated using 1D homogeneous leaf layers fully covering the soil is higher compared to spatially explicit 3D canopies with air gaps (Malenovský et al., 2021; Regaieg et al., 2021, 2023). The canopy cover fraction is a key variable for accurate simulation of SIF radiance and subsequent estimation of FQE. This finding was confirmed by results in Fig. 11, demonstrating that, compared to original genuine canopies, canopies with randomly distributed plants of the same canopy cover but different LAI resulted in a lower relative RMSE of the FQE estimates than canopies of the same LAI but varying canopy cover. Therefore, before the HyPlant FQE retrievals, we estimated the canopy cover fraction along with leaf biochemical traits impacting leaf optical properties in the 400–850 nm spectral range and with a coefficient proportional to actual soil brightness. The strong impact of the canopy cover fraction is highlighted in scatterplots of Fig. 16, suggesting that FQE could be approximated from TOC SIF radiance by multiple linear functions fitted per given canopy cover fraction.

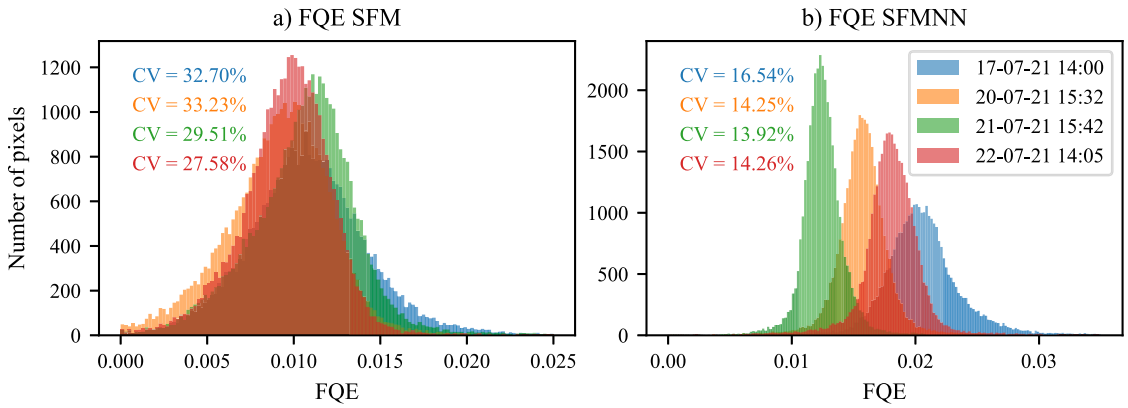

Fig. 15. Histograms of FQE values retrieved from the four HyPlant SFM (a) and SFMNN (b) retrieved TOC SIF radiance acquired on 17th, 20th, 21st, and 22nd July 2021.

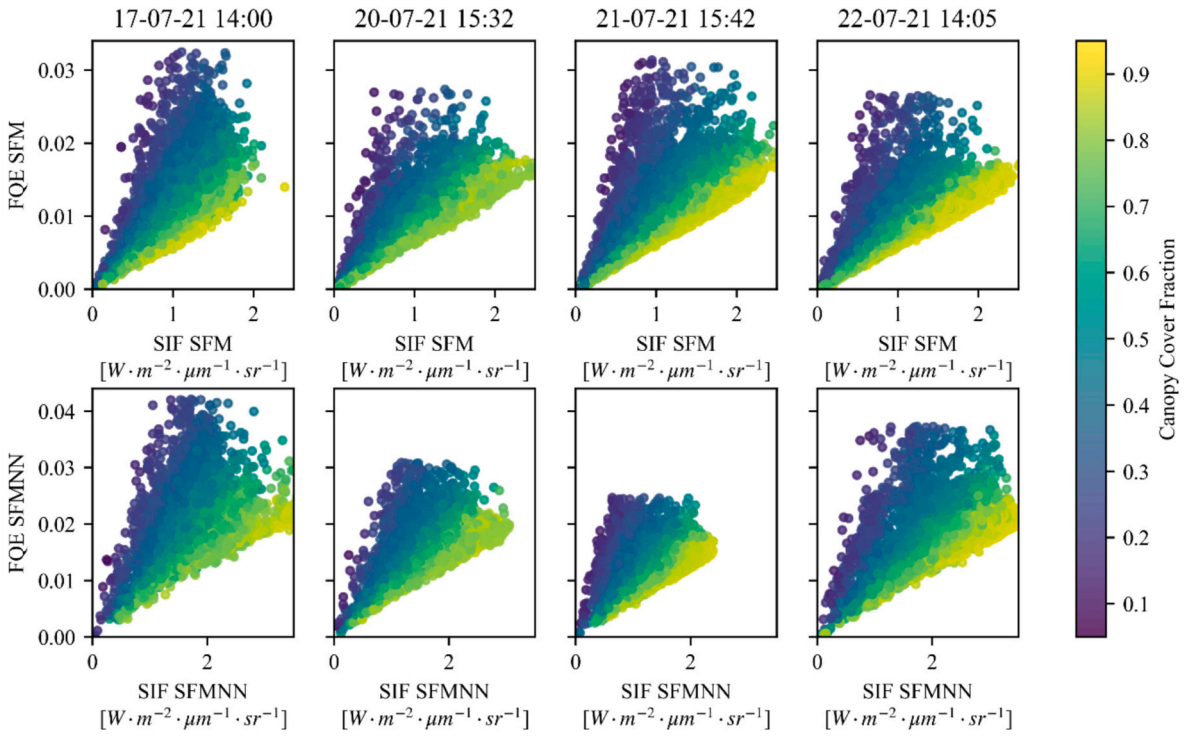

Fig. 16. Scatter plots of TOC SIF radiance *vs.* FQE retrieved from SFM and SFMNN TOC SIF radiance datasets acquired by HyPlant on 17th, 20th, 21st, and 22nd July 2021.

4.3. Performance assessment of the downscaling approach

To assess performance of our downscaling approach, we compared leaf fluorescence efficiencies at 760 nm, computed using the Fluorescence Correction Vegetation Index (FCVI; Yang et al., 2020), with the photosystem-level diurnal FQE values retrieved from FloX measurements. Despite the fact that the two quantities have different physical units and represent different levels of downscaling, we found statistically significant linear relationships ($R^2 > 0.8$) for all six measurement days (see Appendix H). This finding indicates a temporally constant anatomy of the alfalfa leaves, impacting leaf transfer of SIF during the investigated days linearly. It also indicates that the inner structure of leaves is not, in the case of this crop, the major SIF confounding factor. A similar diurnal variation in leaf-level fluorescence efficiency at 760 nm was found for a maize canopy by Yang et al. (2020). Moya et al. (2019) and Loayza et al. (2023) described the diurnal course as "M-shaped", having the second afternoon peak of a lower amplitude after the first maximum occurring in the morning. Additionally, the diurnal trends of FQE retrieved from FloX measurements on 20th, 21st, and 22nd July 2021 (Fig. 8) are in agreement with leaf SIF efficiencies retrieved from drone and HyPlant observations of barley varieties by Bendig et al. (2025). Their diurnal courses showed low stagnating values from late morning until afternoon, followed by a slight increase in SIF efficiencies after 3.00 pm of the local time.

Our FQE estimates were found to be in line also with typical fluorescence yield diurnal variation measured with active chlorophyll fluorescence instruments (ESA, 2015), for instance, with SIF yields of potato crops observed under sunny conditions (Loayza et al., 2023), pea and mint canopies (Moya et al., 2019), and sunflower and hibiscus canopies (Amoros-Lopez et al., 2008). Hence, to further understand the FQE temporal photosynthetic dynamics, we compared their values with the photosynthetic yield of PSII measured for sunlit leaves with a miniaturized pulse-amplitude modulated photosynthesis yield analyzer (Mini-PAM) (Bilger et al., 1995). The scatterplot of the photosynthetic

yield of PSII averaged for sampled sunlit leaves *vs.* the retrieved FQE linearly interpolated for the corresponding time (Appendix I), reveals a changing leaf energy dissipation dynamic throughout the day, as previously reported by Wieneke et al. (2022), Marrs et al. (2020), and van der Tol et al. (2014). While a positive correlation, associated with lower leaf temperatures, was observed in the morning, it turned negative in the afternoon, in correspondence with higher leaf surface temperatures. The positive morning relationship can be attributed to no-stress conditions until the solar noon, when the high irradiance stress conditions resulted in a downregulation of PSII photosynthetic yield. This downregulation is associated with an increase in the non-photochemical quenching (NPQ) protective mechanisms, resulting in a negative FQE-photosynthesis yield relationship. A similar trend was observed during a summer heatwave by Martini et al. (2022).

4.4. Separate estimation of PSI and PSII FQEs

We also estimated the diurnal FQE courses of PSI and PSII from red and far-red SIF radiance peaks separately, by coupling DART with an older version of the Fluspect model using FQE values per photosystem and accepting the assumption that red SIF emission is associated mainly with PSII (Franck et al., 2002; Iriel et al., 2014). Since the red TOC SIF retrieval method is technically challenging and subjected to an intensive chlorophyll reabsorption (Liu et al., 2020; Wu et al., 2024), it is usually accompanied by a higher uncertainty than the far-red SIF retrieval (Cendrero-Mateo et al., 2019; Duan et al., 2022; Rossini et al., 2016). This can explain the higher noise observed in diurnal courses of FloX red SIF when compared to the far-red SIF radiance (Figure 1). Likewise, the estimated FQE of PSII inherited the uncertainties of the red SIF radiance, which then propagated into the complementary FQE estimates of PSI (Fig. 12). Despite the noisiness, red TOC SIF has shown in some studies a high potential for GPP estimation and outperformed in some studies far-red SIF (Duan et al., 2022; Liu et al., 2020; Wu et al., 2024). Recently, the reabsorption-corrected red SIF demonstrated a good potential for tracking drought and heat stress (Wieneke et al., 2024). Therefore, the separately retrieved red and far-red FQEs should be further investigated, as they might be differently sensitive and, hence, suitable for detection of early plant stress events and phenological changes.

4.5. Limitations and potential applications

As discussed in Section 4.1, our downscaling method allows to remove the impact of confounding impacts and normalize the SIF measurements. Although the findings discussed in Section 4.3 suggest satisfactory validity of the method, a proper validation requires simultaneous measurement of photosystem-level FQE of a representative number of leaves, which is practically challenging. The leaf-level FQE could be used as approximation, if a high-throughput instrument capable of measuring about 40–50 leaf optical properties per hour, would be available.

It is important to mention that the potential diurnal variability in leaf angular distribution (LAD) (Rosa and Forseth, 1996) was not considered in our approach, as LAD was defined in each plant 3D object manually based on photographs of representative plants. This limitation should be addressed in the future by including in the DART scene parametrization 3D plant representatives with diurnally varying leaf angular distributions.

The development of this method was motivated by a provision of standardized photosystem-level information from TOC SIF data, directly linked to the photosynthetic activity. This extracted information is comparable across the different spatial and temporal scales of the observation, the canopy structure, and the atmospheric condition, and could be, therefore, used to establish a stronger link between SIF and the vegetation gross primary production the estimation of vegetation GPP (Liu et al., 2020) as well as stress detection, *e.g.*, drought monitoring (Lin et al., 2022).

5. Concluding remarks

In this study, we developed a novel method for scaling vegetation canopy observations of SIF radiance down to the level of photosystems inside chloroplasts based on 3D radiative transfer modeling of DART coupled with the leaf SIF model Fluspect-Cx. The method was successfully applied on *in-situ* FloX SIF temporal measurements, revealing diurnal FQE trends, and on airborne HyPlant SIF images, mapping FQE spatial patterns of an alfalfa crop. We found that our FloX FQE diurnal trends correspond with previously published diurnal courses of the leaf-level SIF efficiency and the PSII fluorescence yield. In contrast to HyPlant TOC SIF radiance, the retrieved FQE maps appeared to be spatially more homogeneous, which corresponds with a spatially uniform photosynthetic performance of the investigated mono-species crop of a single alfalfa variety. These results demonstrate that DART 3D modeling can be used to remove the effects of confounding factors by physically simulating their impacts on TOC SIF radiance, which allows for subsequent extraction of the physiological part of measured canopy SIF signal. As the DART modeling was, except uncertainties related to its parametrization, noiseless, noise and spatial artefacts of retrieved photosystem level FQE estimates were predominantly inherited from the input top-of-the-canopy SIF radiance data. Future methodological improvements should include more genuine representation of 3D vegetation canopy, especially a consideration of the canopy leaf angular variability as response to spatiotemporally varying solar irradiation conditions. Finally, the method is expected to be tested on more spatially heterogenous and architecturally complex canopies, *e.g.*, diverse forest stands, where the 3D structure and non-photosynthetic canopy surfaces (*e.g.*, woody components) have been shown to impose a great impact on spatial anisotropy of TOC SIF signal (Malenovský et al., 2021; Regaieg et al., 2021).

CRediT authorship contribution statement

Omar Regaieg: Writing – original draft, Visualization, Validation, Software, Methodology, Investigation, Data curation. **Zbyněk Malenovský:** Writing – original draft, Supervision, Project administration, Methodology, Conceptualization. **Bastian Siegmann:** Writing – review & editing, Methodology, Investigation. **Jim Buffat:** Writing – original draft, Methodology. **Julie Krämer:** Writing – original draft, Investigation. **Nicolas Lauret:** Software. **Valérie Le Dantec:** Investigation.

Declaration of Competing Interest

The authors declare that they have no known competing financial interests or personal relationships that could have appeared to influence the work reported in this paper.

Acknowledgments

Authors acknowledge the financial support of the French National Agency for Research (CNRS) (grant number ANR-19-01CE-0017 in support of the project “HILIAISE: Human Imprint on Land surface Interactions with the Atmosphere over the Iberian Semi-arid Environment”) that funded the field and airborne campaign. We also gratefully acknowledge computing time on the supercomputer JURECA (Thörnig, 2021) at Forschungszentrum Jülich under grant no. fluomap-ct. Additionally, we thank Thang Quang Nguyen from the Remote Sensing Research Group at the University of Bonn for his support of the MiniPAM fluorescence yield analyses, the DART team, led by Prof. Jean-Philippe Gastellu-Etchegorry at the CESBIO Laboratory (Toulouse, France), for continuous development of the DART model, and Dr. Oscar Hartogensis from Wageningen University & Research (Wageningen, the Netherlands) for providing the PAR data.

Appendix A: Study site location

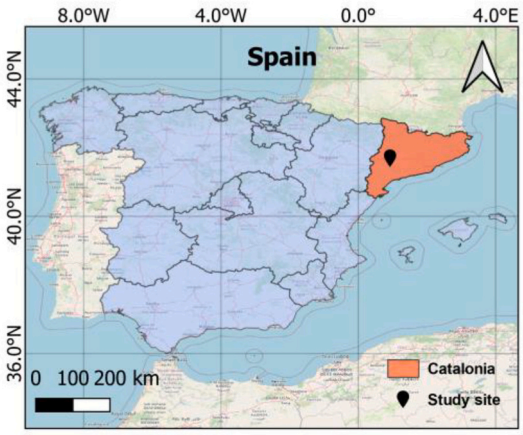

Fig. A1. Study site location (Figure created using OpenStreetMap and shapefiles from https://diva-gis.org/).

Appendix B: Example of total, direct and diffuse DART simulated irradiance (19th July 2021 at 10 am local time)

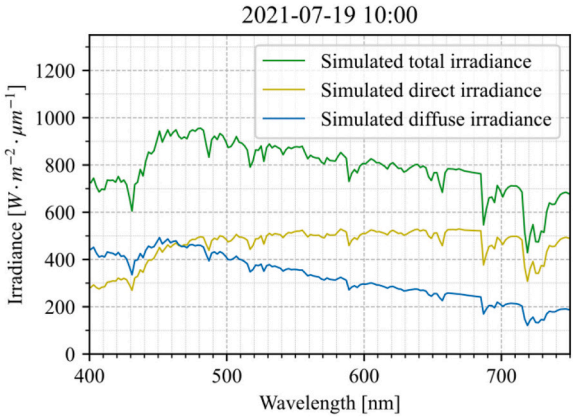

Fig. B1. Total, direct, and diffuse irradiance simulated in DART using retrieved atmospheric optical depths for 19th July 2021 at 10 am (local time).

Appendix C: Soil reflectance spectra

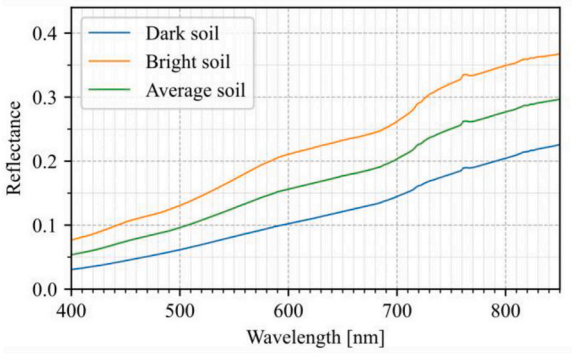

Fig. C1. Reflectance spectra of the dark and bright soils, and their average.

Appendix D. Pseudo code for full field mock-up creation

Input parameters

- Maps of estimated canopy traits
- Prebuilt list L of alfalfa fields of $1.7 \times 1.7\ m^2$ (HyPlant pixel size) having different canopy cover fractions (Fcov) L = [0.05 to 0.95 with a step of approximately 0.05]

Pseudo code:

for each HyPlant image pixel (x,y) of the alfalfa field *do*:
if $\exists field \in L$ such that $|\mathrm{Fcov}(field) - \mathrm{Fcov}(x,y)| < 0.01$:
add a copy c of *field* to the mock-up at position (x,y)
set leaves properties of c and soil optical properties at (x,y)
else:
find $f \in L$ with smallest Fcov such as $\mathrm{Fcov}(f) > \mathrm{Fcov}(x,y)$
repeat
Randomly remove one plant from f to create a new f' compute
Compute $\mathrm{Fcov}(f')$
Add f' to L

$f \leftarrow f'$

until $(|\mathrm{Fcov}(f') - \mathrm{Fcov}(x,y)| < 0.01)$
add a copy c of f' to the mock-up at position (x,y)
set leaves optical properties of c and soil optical properties at (x,y)
end if
end for

Appendix E: Example of leaf/canopy traits maps of the alfalfa field estimated by the best performing ANN for the HyPlant overflight on 22nd July 2021

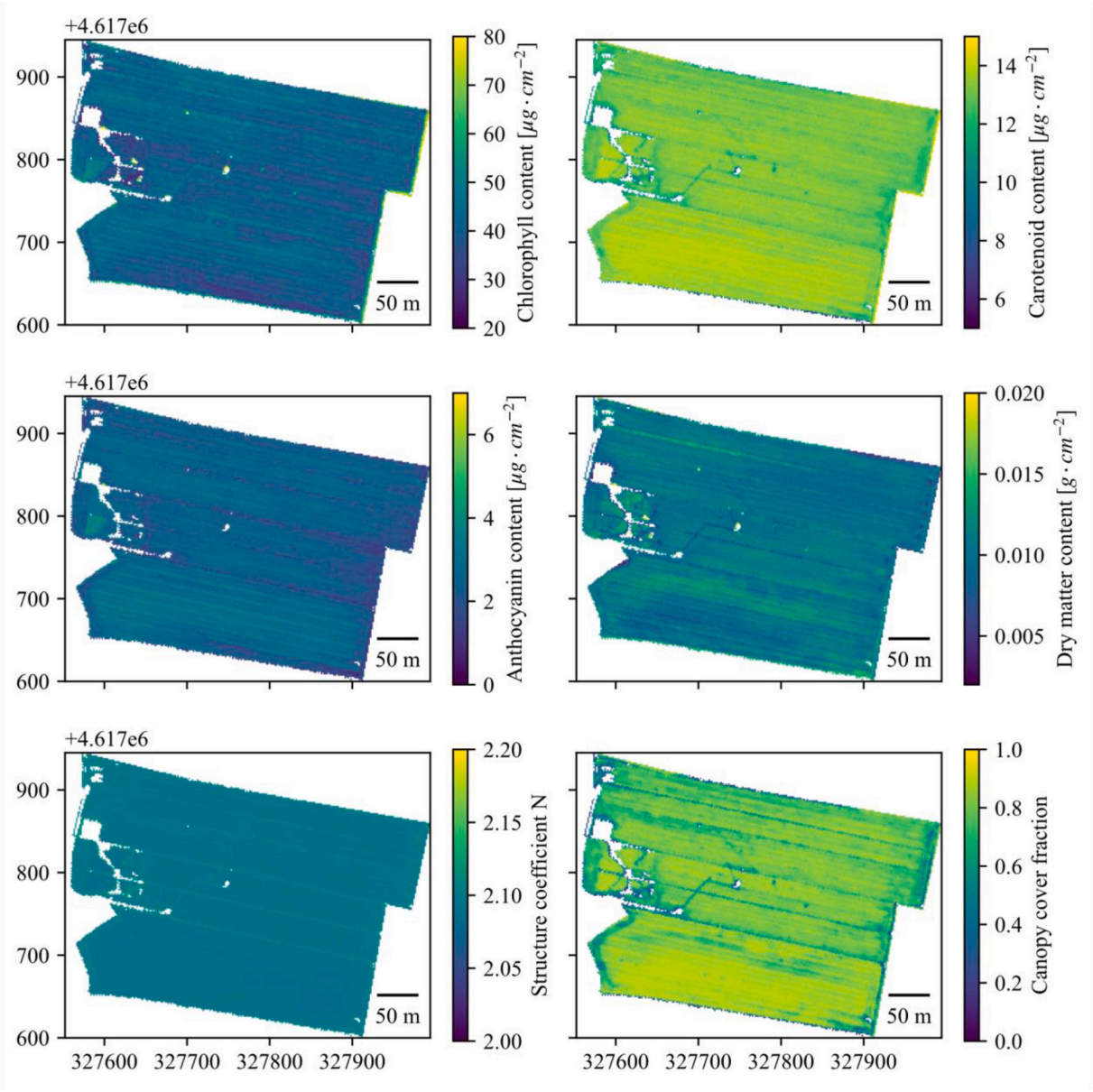

Fig. E1. Examples of maps of alfalfa leaf and canopy traits estimated by the best performing ANN for the HyPlant overflight on 22nd July 2021.

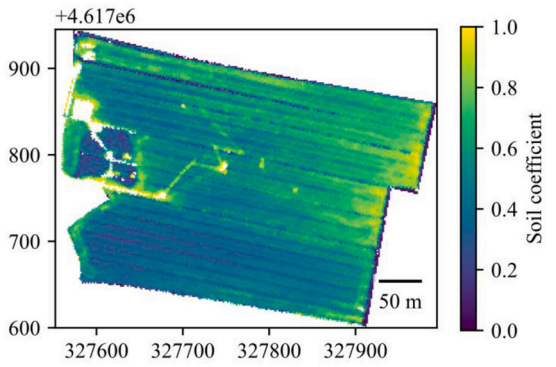

Fig. E2. Example of an alfalfa field soil coefficient map estimated by the best performing ANN for the HyPlant overflight on 22nd July 2021.

Appendix F: DART-Lux iterations of the FQE retrieval method for a Hyplant acquisition

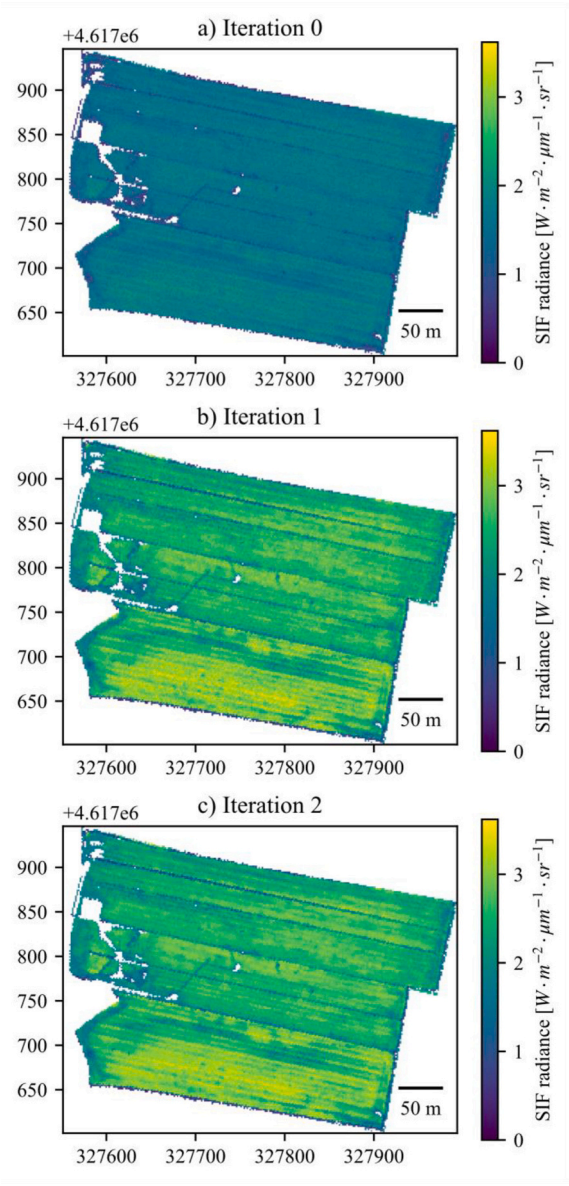

Fig. F1. DART-simulated SIF radiance images at the O2A band: a) iteration 0, simulated using a reference FQE (RMSE = 0.8862 W.m^{-2}.µm^{-1}.sr^{-1}), b) iteration 1, simulated using FQE values adjusted based on iteration 0 (RMSE = 0.0762 W.m^{-2}.µm^{-1}.sr^{-1}), and c) iteration 2, simulated using FQEs readjusted based on iteration 1 (RMSE = 0.0064 W.m^{-2}.µm^{-1}.sr^{-1}). RMSEs were computed with the SFMNN-retrieved HyPlant O_2A SIF radiances from 22nd July 2021 as the reference.

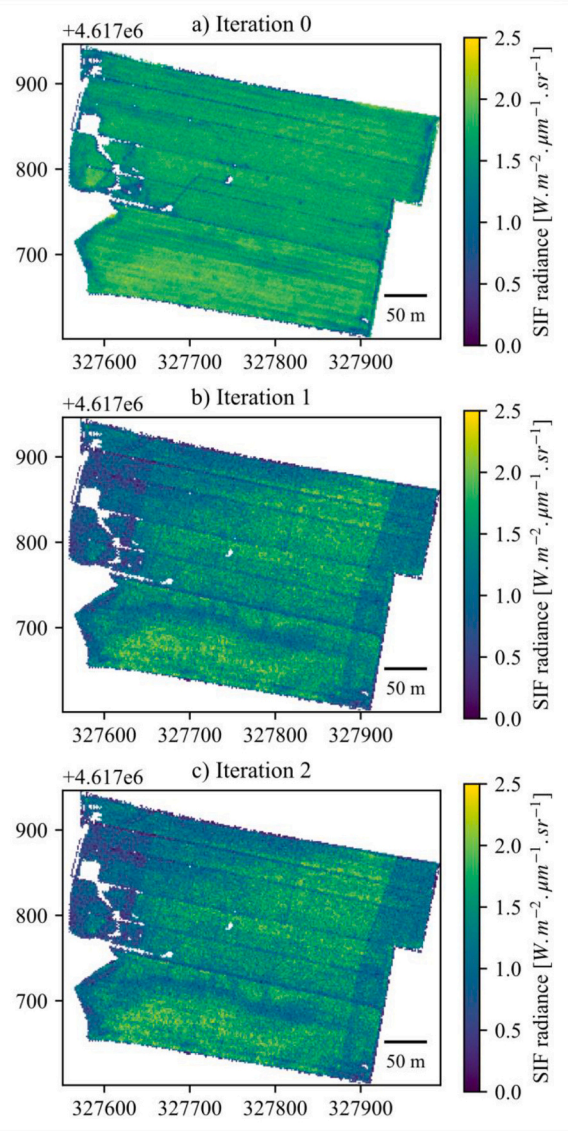

Fig. F2. DART-simulated SIF radiance images at the O_2A band: a) iteration 0, simulated using a reference FQE (RMSE = 0.4609 $W.m^{-2}.\mu m^{-1}.sr^{-1}$), b) iteration 1, simulated using FQE values adjusted based on iteration 0 (RMSE = 0.0440 $W.m^{-2}.\mu m^{-1}.sr^{-1}$), and c) iteration 2, simulated using FQEs readjusted based on iteration 1 (RMSE = 0.0040 $W.m^{-2}.\mu m^{-1}.sr^{-1}$). RMSEs were computed with the SFM-retrieved HyPlant O_2A SIF radiances from 22nd July 2021 as the reference.

Appendix G: Comparison between SFM and SFMNN SIF radiance at 760 nm and FQE retrieved from HyPlant overflights

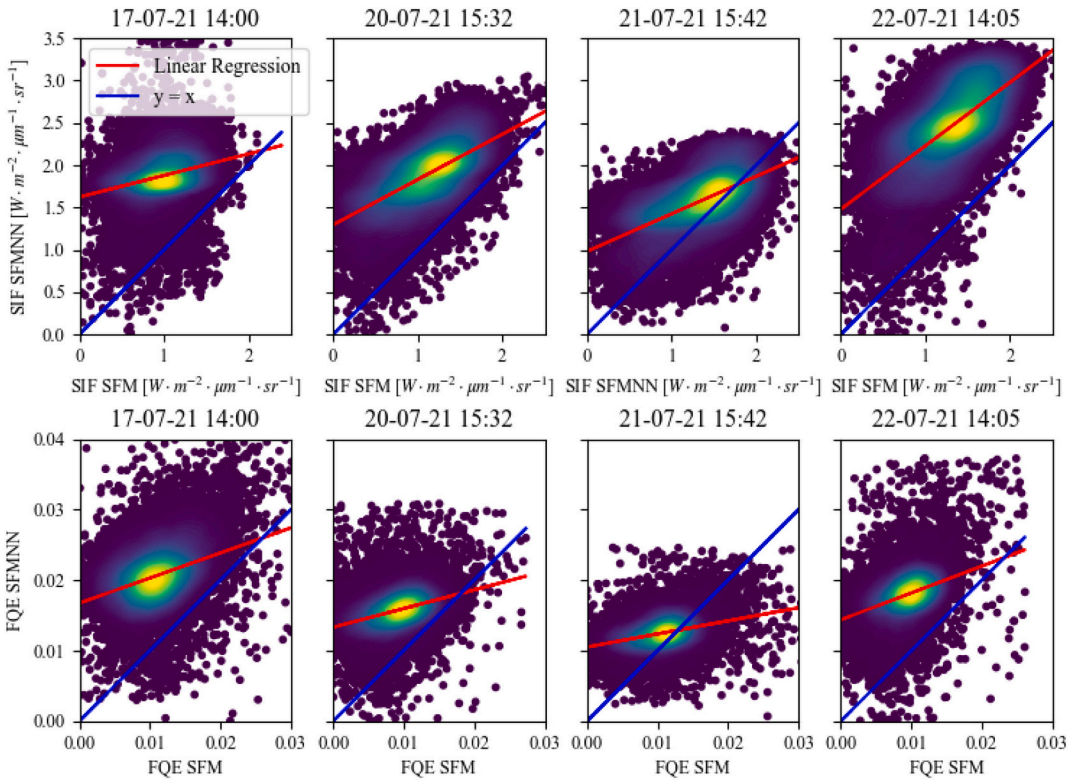

Fig. G1. Scatterplots of SIF radiance calculated using the SFM and SFMNN methods, and of FQE retrieved from SFM and SFMNN SIF radiance values for four HyPlant acquisitions obtained on 17th, 20th, 21st, and 22nd July 2021.

Appendix H: Relationship between the FCVI-estimated leaf-level fluorescence efficiency and the photosystem-level FQE

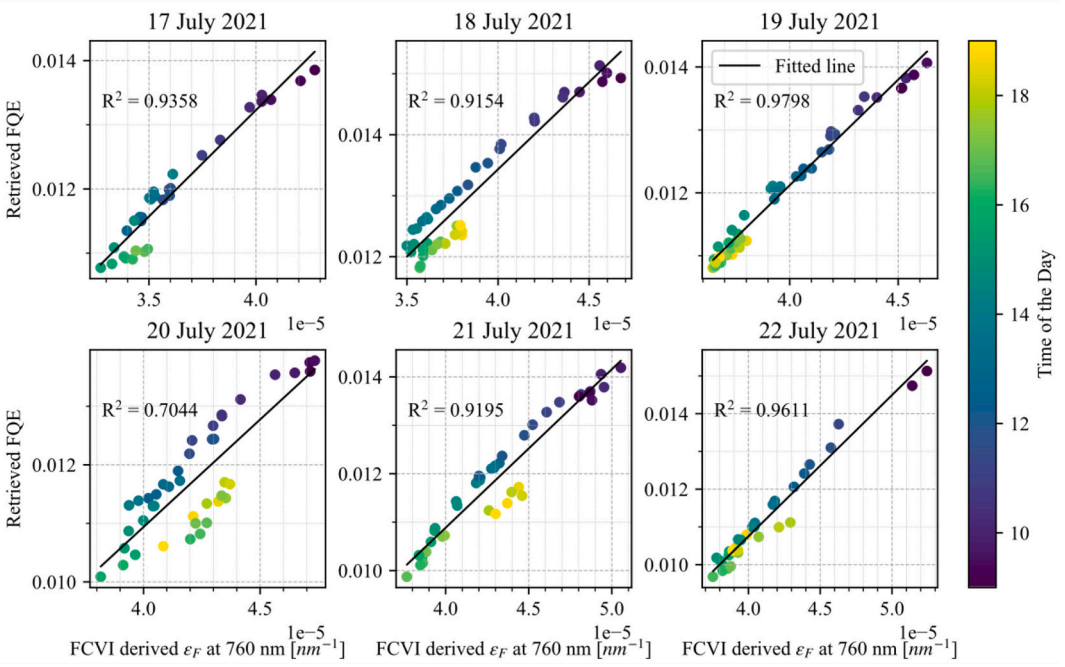

Fig. H1. Regressive relationship between leaf-level fluorescence efficiency at 760 nm, estimated using the reflectance index FCVI and the photosystem-level FQE.

Appendix I: Correlations between measured PSII photosynthetic activity and estimated FQE

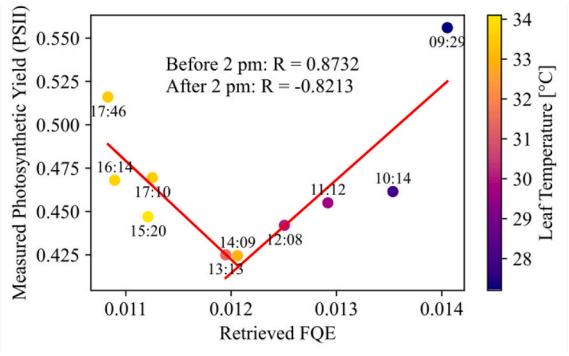

Fig. I1. Scatterplot of the FQE values retrieved from FloX measurements plotted against the photosynthetic yields for photosystem II (PSII) measured with a MiniPAM device. The two red lines (linear fitting) indicate a positive correlation before and a negative correlation after 2.00 pm, respectively (a local time is noted next to datapoints). R is the coefficient of correlation. The color of datapoints indicates the leaf surface temperature as measured by a MiniPAM contact probe. (For interpretation of the references to color in this figure legend, the reader is referred to the web version of this article.)

Appendix J. Supplementary data

Supplementary data to this article can be found online at https://doi.org/10.1016/j.rse.2025.114636.

Data availability

Data will be made available on request.

References

Ač, A., Malenovský, Z., Olejníčková, J., Gallé, A., Rascher, U., Mohammed, G., 2015. Meta-analysis assessing potential of steady-state chlorophyll fluorescence for remote sensing detection of plant water, temperature and nitrogen stress. Remote Sens. Environ. 168, 420–436. https://doi.org/10.1016/j.rse.2015.07.022.

Amoros-Lopez, J., Gomez-Chova, L., Vila-Frances, J., Alonso, L., Calpe, J., Moreno, J., del Valle-Tascon, S., 2008. Evaluation of remote sensing of vegetation fluorescence by the analysis of diurnal cycles. International Journal of Remote Sensing 29 (17–18), 5423–5436. https://doi.org/10.1080/01431160802036391.

Badgley, G., Field, C.B., Berry, J.A., 2017. Canopy near-infrared reflectance and terrestrial photosynthesis. Sci. Adv. 3 (3), e1602244. https://doi.org/10.1126/sciadv.1602244.

Bendig, J., Malenovský, Z., Siegmann, B., Krämer, J., Rascher, U., 2025. Comparing methods for solar-induced fluorescence efficiency estimation using radiative transfer modelling and airborne diurnal measurements of barley crops. Remote Sens. Environ. 317, 114521. https://doi.org/10.1016/j.rse.2024.114521.

Bilger, W., Schreiber, U., Bock, M., 1995. Determination of the quantum efficiency of photosystem II and of non-photochemical quenching of chlorophyll fluorescence in the field. Oecologia 102 (4), 425–432. https://doi.org/10.1007/BF00341354.

Boitard, P., Coudert, B., Lauret, N., Queguiner, S., Marais-Sicre, C., Regaieg, O., Wang, Y., Gastellu-Etchegorry, J.-P., 2023. Calibration of DART 3D model with UAV and Sentinel-2 for studying the radiative budget of conventional and agro-ecological maize fields. Remote Sensing Applications: Society and Environment 32, 101079. https://doi.org/10.1016/j.rsase.2023.101079.

Buffat, J., Pato, M., Alonso, K., Auer, S., Carmona, E., Maier, S., Müller, R., Rademske, P., Siegmann, B., Rascher, U., Scharr, H., 2025. A multi-layer perceptron approach for SIF retrieval in the O2-a absorption band from hyperspectral imagery of the airborne HyPlant sensor system. Remote Sens. Environ. 318, 114596. https://doi.org/10.1016/j.rse.2024.114596.

Campbell, P.K.E., Middleton, E.M., Corp, L.A., Kim, M.S., 2008. Contribution of chlorophyll fluorescence to the apparent vegetation reflectance. Sci. Total Environ. 404 (2), 433–439. https://doi.org/10.1016/j.scitotenv.2007.11.004.

Celesti, M., van der Tol, C., Cogliati, S., Panigada, C., Yang, P., Pinto, F., Rascher, U., Miglietta, F., Colombo, R., Rossini, M., 2018. Exploring the physiological information of sun-induced chlorophyll fluorescence through radiative transfer model inversion. Remote Sens. Environ. 215, 97–108. https://doi.org/10.1016/j.rse.2018.05.013.

Cendrero-Mateo, M.P., Wieneke, S., Damm, A., Alonso, L., Pinto, F., Moreno, J., Guanter, L., Celesti, M., Rossini, M., Sabater, N., Cogliati, S., Julitta, T., Rascher, U., Goulas, Y., Aasen, H., Pacheco-Labrador, J., Mac Arthur, A., 2019. Sun-induced chlorophyll fluorescence III: benchmarking retrieval methods and sensor characteristics for proximal sensing. Remote Sens. (Basel) 11 (8). https://doi.org/10.3390/rs11080962. Article 8.

Cogliati, S., Rossini, M., Julitta, T., Meroni, M., Schickling, A., Burkart, A., Pinto, F., Rascher, U., Colombo, R., 2015a. Continuous and long-term measurements of reflectance and sun-induced chlorophyll fluorescence by using novel automated field spectroscopy systems. Remote Sens. Environ. 164, 270–281. https://doi.org/10.1016/j.rse.2015.03.027.

Cogliati, S., Verhoef, W., Kraft, S., Sabater, N., Alonso, L., Vicent, J., Moreno, J., Drusch, M., Colombo, R., 2015b. Retrieval of sun-induced fluorescence using advanced spectral fitting methods. Remote Sens. Environ. 169, 344–357. https://doi.org/10.1016/j.rse.2015.08.022.

Cogliati, S., Celesti, M., Cesana, I., Miglietta, F., Genesio, L., Julitta, T., Schuettemeyer, D., Drusch, M., Rascher, U., Jurado, P., Colombo, R., 2019. A spectral fitting algorithm to retrieve the fluorescence Spectrum from canopy radiance. Remote Sens. (Basel) 11 (16). https://doi.org/10.3390/rs11161840. Article 16.

Duan, W., Liu, X., Chen, J., Du, S., Liu, L., Jing, X., 2022. Investigating the performance of red and far-red SIF for monitoring GPP of alpine meadow ecosystems. Remote Sens. (Basel) 14 (12). https://doi.org/10.3390/rs14122740. Article 12.

ESA, 2015. Report for Mission Selection: FLEX (ESA SP-1330/2). https://esamultimedia.esa.int/docs/EarthObservation/SP1330-2_FLEX.pdf.

Fournier, A., Daumard, F., Champagne, S., Ounis, A., Goulas, Y., Moya, I., 2012. Effect of canopy structure on sun-induced chlorophyll fluorescence. ISPRS J. Photogramm. Remote Sens. 68, 112–120. https://doi.org/10.1016/j.isprsjprs.2012.01.003.

Franck, F., Juneau, P., Popovic, R., 2002. Resolution of the photosystem I and photosystem II contributions to chlorophyll fluorescence of intact leaves at room temperature. Biochimica et Biophysica Acta (BBA) - Bioenergetics 1556 (2), 239–246. https://doi.org/10.1016/S0005-2728(02)00366-3.

Frankenberg, C., Fisher, J.B., Worden, J., Badgley, G., Saatchi, S.S., Lee, J.-E., Toon, G.C., Butz, A., Jung, M., Kuze, A., Yokota, T., 2011. New global observations of the terrestrial carbon cycle from GOSAT: patterns of plant fluorescence with gross primary productivity. Geophys. Res. Lett. 38 (17). https://doi.org/10.1029/2011GL048738.

Frankenberg, C., Köhler, P., Magney, T.S., Geier, S., Lawson, P., Schwochert, M., McDuffie, J., Drewry, D.T., Pavlick, R., Kuhnert, A., 2018. The chlorophyll fluorescence imaging spectrometer (CFIS), mapping far red fluorescence from aircraft. Remote Sens. Environ. 217, 523–536. https://doi.org/10.1016/j.rse.2018.08.032.

Gastellu-Etchegorry, J.-P., Lauret, N., Yin, T., Landier, L., Kallel, A., Malenovský, Z., Bitar, A.A., Aval, J., Benhmida, S., Qi, J., Medjdoub, G., Guilleux, J., Chavanon, E., Cook, B., Morton, D., Chrysoulakis, N., Mitraka, Z., 2017. DART: Recent advances in remote sensing data modeling with atmosphere, polarization, and chlorophyll fluorescence. In: IEEE Journal of Selected Topics in Applied Earth Observations and Remote Sensing, 10(6), 2640–2649. https://doi.org/10.1109/JSTARS.2017.2685528.

Guanter, L., Zhang, Y., Jung, M., Joiner, J., Voigt, M., Berry, J.A., Frankenberg, C., Huete, A.R., Zarco-Tejada, P., Lee, J.-E., Moran, M.S., Ponce-Campos, G., Beer, C., Camps-Valls, G., Buchmann, N., Gianelle, D., Klumpp, K., Cescatti, A., Baker, J.M., Griffis, T.J., 2014. Global and time-resolved monitoring of crop photosynthesis with chlorophyll fluorescence. Proc. Natl. Acad. Sci. 111 (14), E1327–E1333. https://doi.org/10.1073/pnas.1320008111.

Guanter, L., Bacour, C., Schneider, A., Aben, I., van Kempen, T.A., Maignan, F., Retscher, C., Köhler, P., Frankenberg, C., Joiner, J., Zhang, Y., 2021. The TROPOSIF global sun-induced fluorescence dataset from the sentinel-5P TROPOMI mission. Earth System Science Data 13 (11), 5423–5440. https://doi.org/10.5194/essd-13-5423-2021.

Hu, M., Cheng, X., Zhang, J., Huang, H., Zhou, Y., Wang, X., Pan, Q., Guan, C., 2023. Temporal variation in tower-based solar-induced chlorophyll fluorescence and its environmental response in a Chinese Cork oak plantation. Remote Sens. (Basel) 15 (14), Article 14. https://doi.org/10.3390/rs15143568.

Iriel, A., Novo, J.M., Cordon, G.B., Lagorio, M.G., 2014. Atrazine and methyl Viologen effects on chlorophyll-a fluorescence revisited—implications in photosystems emission and Ecotoxicity assessment. Photochem. Photobiol. 90 (1), 107–112. https://doi.org/10.1111/php.12142.

Jacquemoud, S., Ustin, S.L., Verdebout, J., Schmuck, G., Andreoli, G., Hosgood, B., 1996. Estimating leaf biochemistry using the PROSPECT leaf optical properties model. Remote Sens. Environ. 56 (3), 194–202. https://doi.org/10.1016/0034-4257(95)00238-3.

Knyazikhin, Y., Schull, M.A., Xu, L., Myneni, R.B., Samanta, A., 2011. Canopy spectral invariants. Part 1: a new concept in remote sensing of vegetation. J. Quant. Spectrosc. Radiat. Transf. 112 (4), 727–735. https://doi.org/10.1016/j.jqsrt.2010.06.014.

Lamsal, K., Malenovský, Z., Woodgate, W., Waterman, M., Brodribb, T.J., Aryal, J., 2022. Spectral retrieval of eucalypt leaf biochemical traits by inversion of the Fluspect-cx model. Remote Sens. (Basel) 14 (3). https://doi.org/10.3390/rs14030567. Article 3.

Lin, J., Shen, Q., Wu, J., Zhao, W., Liu, L., 2022. Assessing the potential of downscaled far red solar-induced chlorophyll fluorescence from the canopy to leaf level for drought monitoring in winter wheat. Remote Sens. (Basel) 14 (6). https://doi.org/10.3390/rs14061357. Article 6.

Liu, X., Liu, L., Zhang, S., Zhou, X., 2015. New spectral fitting method for full-Spectrum solar-induced chlorophyll fluorescence retrieval based on principal components analysis. Remote Sens. (Basel) 7 (8). https://doi.org/10.3390/rs70810626. Article 8.

Liu, X., Guanter, L., Liu, L., Damm, A., Malenovský, Z., Rascher, U., Peng, D., Du, S., Gastellu-Etchegorry, J.-P., 2019a. Downscaling of solar-induced chlorophyll fluorescence from canopy level to photosystem level using a random forest model. Remote Sens. Environ. 231, 110772. https://doi.org/10.1016/j.rse.2018.05.035.

Liu, X., Liu, L., Hu, J., Guo, J., Du, S., 2020. Improving the potential of red SIF for estimating GPP by downscaling from the canopy level to the photosystem level. Agric. For. Meteorol. 281, 107846. https://doi.org/10.1016/j.agrformet.2019.107846.

Liu, Z., Lu, X., An, S., Heskel, M., Yang, H., Tang, J., 2019b. Advantage of multi-band solar-induced chlorophyll fluorescence to derive canopy photosynthesis in a temperate forest. Agric. For. Meteorol. 279, 107691. https://doi.org/10.1016/j.agrformet.2019.107691.

Loayza, H., Moya, I., Quiroz, R., Ounis, A., Goulas, Y., 2023. Active and passive chlorophyll fluorescence measurements at canopy level on potato crops. Evidence of similitude of diurnal cycles of apparent fluorescence yields. Photosynth. Res. 155 (3), 271–288. https://doi.org/10.1007/s11120-022-00995-8.

Malenovský, Z., Albrechtová, J., Lhoták ová, Z., Zurita-Milla, R., Clevers, J.G.P.W., Schaepman, M.E., Cudlín, P., 2006. Applicability of the PROSPECT model for Norway spruce needles. Int. J. Remote Sens. 27 (24), 5315–5340. https://doi.org/10.1080/01431160600762990.

Malenovský, Z., Regaieg, O., Yin, T., Lauret, N., Guilleux, J., Chavanon, E., Duran, N., Janoutová, R., Delavois, A., Meynier, J., Medjdoub, G., Yang, P., van der Tol, C., Morton, D., Cook, B.D., Gastellu-Etchegorry, J.-P., 2021. Discrete anisotropic radiative transfer modelling of solar-induced chlorophyll fluorescence: structural impacts in geometrically explicit vegetation canopies. Remote Sens. Environ. 263, 112564. https://doi.org/10.1016/j.rse.2021.112564.

Marrs, J.K., Reblin, J.S., Logan, B.A., Allen, D.W., Reinmann, A.B., Bombard, D.M., Tabachnik, D., Hutyra, L.R., 2020. Solar-induced fluorescence does not track photosynthetic carbon assimilation following induced stomatal closure. Geophys. Res. Lett. 47 (15), e2020GL087956. https://doi.org/10.1029/2020GL087956.

Martini, D., Sakowska, K., Wohlfahrt, G., Pacheco-Labrador, J., van der Tol, C., Porcar-Castell, A., Magney, T.S., Carrara, A., Colombo, R., El-Madany, T.S., Gonzalez-Cascon, R., Martín, M.P., Julitta, T., Moreno, G., Rascher, U., Reichstein, M., Rossini, M., Migliavacca, M., 2022. Heatwave breaks down the linearity between sun-induced fluorescence and gross primary production. New Phytol. 233 (6), 2415–2428. https://doi.org/10.1111/nph.17920.

Mohammed, G.H., Colombo, R., Middleton, E.M., Rascher, U., van der Tol, C., Nedbal, L., Goulas, Y., Pérez-Priego, O., Damm, A., Meroni, M., Joiner, J., Cogliati, S., Verhoef, W., Malenovský, Z., Gastellu-Etchegorry, J.-P., Miller, J.R., Guanter, L., Moreno, J., Moya, I., Zarco-Tejada, P.J., 2019. Remote sensing of solar-induced chlorophyll fluorescence (SIF) in vegetation: 50 years of progress. Remote Sens. Environ. 231, 111177. https://doi.org/10.1016/j.rse.2019.04.030.

Moya, I., Loayza, H., López, M.L., Quiroz, R., Ounis, A., Goulas, Y., 2019. Canopy chlorophyll fluorescence applied to stress detection using an easy-to-build micro-lidar. Photosynth. Res. 142 (1), 1–15. https://doi.org/10.1007/s11120-019-00642-9.

Naethe, P., De Sanctis, A., Burkart, A., Campbell, P.K.E., Colombo, R., Di Mauro, B., Damm, A., El-Madany, T., Fava, F., Gamon, J.A., Huemmrich, K.F., Migliavacca, M., Paul-Limoges, E., Rascher, U., Rossini, M., Schüttemeyer, D., Tagliabue, G., Zhang, Y., Julitta, T., 2024. Towards a standardized, ground-based network of hyperspectral measurements: combining time series from autonomous field spectrometers with Sentinel-2. Remote Sens. Environ. 303, 114013. https://doi.org/10.1016/j.rse.2024.114013.

Porcar-Castell, A., Malenovský, Z., Magney, T., Van Wittenberghe, S., Fernández-Marín, B., Maignan, F., Zhang, Y., Maseyk, K., Atherton, J., Albert, L.P., Robson, T. M., Zhao, F., Garcia-Plazaola, J.-I., Ensminger, I., Rajewicz, P.A., Grebe, S., Tikkanen, M., Kellner, J.R., Ihalainen, J.A., Logan, B., 2021. Chlorophyll a fluorescence illuminates a path connecting plant molecular biology to earth-system science. Nature Plants 7 (8), 998–1009. https://doi.org/10.1038/s41477-021-00980-4.

Rascher, U., Alonso, L., Burkart, A., Cilia, C., Cogliati, S., Colombo, R., Damm, A., Drusch, M., Guanter, L., Hanus, J., Hyvärinen, T., Julitta, T., Jussila, J., Kataja, K., Kokkalis, P., Kraft, S., Kraska, T., Matveeva, M., Moreno, J., Zemek, F., 2015. Sun-induced fluorescence – a new probe of photosynthesis: first maps from the imaging spectrometer HyPlant. Glob. Chang. Biol. 21 (12), 4673–4684. https://doi.org/10.1111/gcb.13017.

Regaieg, O., Yin, T., Malenovský, Z., Cook, B.D., Morton, D.C., Gastellu-Etchegorry, J.-P., 2021. Assessing impacts of canopy 3D structure on chlorophyll fluorescence radiance and radiative budget of deciduous forest stands using DART. Remote Sens. Environ. 265, 112673. https://doi.org/10.1016/j.rse.2021.112673.

Regaieg, O., Lauret, N., Wang, Y., Guilleux, J., Chavanon, E., Gastellu-Etchegorry, J.-P., 2023. Bi-directional Monte-Carlo modelling of solar-induced chlorophyll fluorescence images for 3D vegetation canopies in the DART model. Int. J. Appl. Earth Obs. Geoinf. 118, 103254. https://doi.org/10.1016/j.jag.2023.103254.

Rosa, L.M., Forseth, I.N., 1996. Diurnal patterns of soybean leaf inclination angles and azimuthal orientation under different levels of ultraviolet-B radiation. Agric. For. Meteorol. 78 (1), 107–119. https://doi.org/10.1016/0168-1923(95)02249-X.

Rossini, M., Meroni, M., Celesti, M., Cogliati, S., Julitta, T., Panigada, C., Rascher, U., Van der Tol, C., Colombo, R., 2016. Analysis of red and far-red sun-induced chlorophyll fluorescence and their ratio in different canopies based on observed and modeled data. Remote Sensing 8 (5). https://doi.org/10.3390/rs8050412. Article 5.

Scodellaro, R., Cesana, I., D'Alfonso, L., Bouzin, M., Collini, M., Chirico, G., Colombo, R., Miglietta, F., Celesti, M., Schuettemeyer, D., Cogliati, S., Sironi, L., 2022. A novel hybrid machine learning phasor-based approach to retrieve a full set of solar-induced fluorescence metrics and biophysical parameters. Remote Sens. Environ. 280, 113196. https://doi.org/10.1016/j.rse.2022.113196.

Siegmann, B., Alonso, L., Celesti, M., Cogliati, S., Colombo, R., Damm, A., Douglas, S., Guanter, L., Hanuš, J., Kataja, K., Kraska, T., Matveeva, M., Moreno, J., Muller, O., Pikl, M., Pinto, F., Quirós Vargas, J., Rademske, P., Rodriguez-Morene, F., Rascher, U., 2019. The high-performance airborne imaging spectrometer HyPlant—from raw images to top-of-canopy reflectance and fluorescence products: Introduction of an automatized processing chain. Remote Sens. (Basel) 11 (23). https://doi.org/10.3390/rs11232760. Article 23.

Song, L., Guanter, L., Guan, K., You, L., Huete, A., Ju, W., Zhang, Y., 2018. Satellite sun-induced chlorophyll fluorescence detects early response of winter wheat to heat stress in the Indian indo-Gangetic Plains. Glob. Chang. Biol. 24 (9), 4023–4037. https://doi.org/10.1111/gcb.14302.

Tagliabue, G., Panigada, C., Dechant, B., Baret, F., Cogliati, S., Colombo, R., Migliavacca, M., Rademske, P., Schickling, A., Schüttemeyer, D., Verrelst, J., Rascher, U., Ryu, Y., Rossini, M., 2019. Exploring the spatial relationship between airborne-derived red and far-red sun-induced fluorescence and process-based GPP estimates in a forest ecosystem. Remote Sens. Environ. 231, 111272. https://doi.org/10.1016/j.rse.2019.111272.

Thörnig, P., 2021. JURECA: data centric and booster modules implementing the modular supercomputing architecture at Jülich supercomputing Centre. Journal of Large-Scale Research Facilities JLSRF 7, A182. https://doi.org/10.17815/jlsrf-7-182.

van der Tol, C., Verhoef, W., Timmermans, J., Verhoef, A., Su, Z., 2009. An integrated model of soil-canopy spectral radiances, photosynthesis, fluorescence, temperature and energy balance. Biogeosciences 6 (12), 3109–3129. https://doi.org/10.5194/bg-6-3109-2009.

van der Tol, C., Berry, J.A., Campbell, P.K.E., Rascher, U., 2014. Models of fluorescence and photosynthesis for interpreting measurements of solar-induced chlorophyll fluorescence. J. Geophys. Res. Biogeo. 119 (12), 2312–2327. https://doi.org/10.1002/2014JG002713.

Verrelst, J., Rivera, J.P., van der Tol, C., Magnani, F., Mohammed, G., Moreno, J., 2015. Global sensitivity analysis of the SCOPE model: what drives simulated canopy-leaving sun-induced fluorescence? Remote Sens. Environ. 166, 8–21. https://doi.org/10.1016/j.rse.2015.06.002.

Vilfan, N., van der Tol, C., Muller, O., Rascher, U., Verhoef, W., 2016. Fluspect-B: a model for leaf fluorescence, reflectance and transmittance spectra. Remote Sens. Environ. 186, 596–615. https://doi.org/10.1016/j.rse.2016.09.017.

Vilfan, N., Van der Tol, C., Yang, P., Wyber, R., Malenovský, Z., Robinson, S.A., Verhoef, W., 2018. Extending Fluspect to simulate xanthophyll driven leaf reflectance dynamics. Remote Sens. Environ. 211, 345–356. https://doi.org/10.1016/j.rse.2018.04.012.

Wang, Y., Grimaldi, J., Landier, L., Chavanon, E., Gastellu-Etchegorry, J.P., 2020. INTRODUCTION OF CLOUDS IN DART MODEL. In: *The International Archives of the Photogrammetry, Remote Sensing and Spatial Information Sciences, XLIII-B3–2020*, 843–848. XXIV ISPRS Congress, Commission III (Volume XLIII-B3–2020) - 2020 edition. https://doi.org/10.5194/isprs-archives-XLIII-B3-2020-843-2020.

Wang, Y., Kallel, A., Yang, X., Regaieg, O., Lauret, N., Guilleux, J., Chavanon, E., Gastellu-Etchegorry, J.-P., 2022. DART-lux: An unbiased and rapid Monte Carlo radiative transfer method for simulating remote sensing images. Remote Sens. Environ. 274, 112973. https://doi.org/10.1016/j.rse.2022.112973.

Wieneke, S., Balzarolo, M., Asard, H., Abd Elgawad, H., Peñuelas, J., Rascher, U., Ven, A., Verlinden, M.S., Janssens, I.A., Vicca, S., 2022. Fluorescence ratio and photochemical reflectance index as a proxy for photosynthetic quantum efficiency of photosystem II along a phosphorus gradient. Agric. For. Meteorol. 322, 109019. https://doi.org/10.1016/j.agrformet.2022.109019.

Wieneke, S., Pacheco-Labrador, J., Mahecha, M.D., Poblador, S., Vicca, S., Janssens, I.A., 2024. Comparing the quantum use efficiency of red and far-red sun-induced fluorescence at leaf and canopy under heat-drought stress. Remote Sens. Environ. 311, 114294. https://doi.org/10.1016/j.rse.2024.114294.

Wu, L., Zhang, Y., Zhang, Z., Zhang, X., Wu, Y., Chen, J.M., 2024. Deriving photosystem-level red chlorophyll fluorescence emission by combining leaf chlorophyll content

and canopy far-red solar-induced fluorescence: possibilities and challenges. Remote Sens. Environ. 304, 114043. https://doi.org/10.1016/j.rse.2024.114043.
Yang, P., van der Tol, C., 2018. Linking canopy scattering of far-red sun-induced chlorophyll fluorescence with reflectance. Remote Sens. Environ. 209, 456–467. https://doi.org/10.1016/j.rse.2018.02.029.
Yang, P., van der Tol, C., Campbell, P.K.E., Middleton, E.M., 2020. Fluorescence correction vegetation index (FCVI): a physically based reflectance index to separate physiological and non-physiological information in far-red sun-induced chlorophyll fluorescence. Remote Sens. Environ. 240, 111676. https://doi.org/10.1016/j.rse.2020.111676.
Yang, P., van der Tol, C., Campbell, P.K.E., Middleton, E.M., 2021. Unraveling the physical and physiological basis for the solar- induced chlorophyll fluorescence and photosynthesis relationship using continuous leaf and canopy measurements of a corn crop. Biogeosciences 18 (2), 441–465. https://doi.org/10.5194/bg-18-441-2021.
Zeng, Y., Badgley, G., Dechant, B., Ryu, Y., Chen, M., Berry, J.A., 2019. A practical approach for estimating the escape ratio of near-infrared solar-induced chlorophyll fluorescence. Remote Sens. Environ. 232, 111209. https://doi.org/10.1016/j.rse.2019.05.028.
Zeng, Y., Hao, D., Badgley, G., Damm, A., Rascher, U., Ryu, Y., Johnson, J., Krieger, V., Wu, S., Qiu, H., Liu, Y., Berry, J.A., Chen, M., 2021. Estimating near-infrared reflectance of vegetation from hyperspectral data. Remote Sens. Environ. 267, 112723. https://doi.org/10.1016/j.rse.2021.112723.
Zhao, F., Li, R., Verhoef, W., Cogliati, S., Liu, X., Huang, Y., Guo, Y., Huang, J., 2018. Reconstruction of the full spectrum of solar-induced chlorophyll fluorescence: Intercomparison study for a novel method. Remote Sens. Environ. 219, 233–246. https://doi.org/10.1016/j.rse.2018.10.021.
Zhao, F., Ma, W., Zhao, J., Guo, Y., Tariq, M., Li, J., 2024. Global retrieval of the spectrum of terrestrial chlorophyll fluorescence: first results with TROPOMI. Remote Sens. Environ. 300, 113903. https://doi.org/10.1016/j.rse.2023.113903.